6 Image Visualization and Post-processing Techniques

Thomas Flohr and Bernd Ohnesorge

Contents

The application of imaging techniques to original axial images of a CT scan in order to derive additional information or hide unwanted information that distracts from the clinical findings is called image post-processing. Image post-processing requires modification of a 3D image volume, which in most cases consists of a stack of individual axial images. The fundamental 3D unit in this volume is called a «voxel». Ideally, volume image data are of high spatial resolution and isotropic in nature, i.e., each voxel is of equal dimensions in all three spatial axes, and forms the basis for image display in arbitrarily oriented imaging planes and advanced image post-processing techniques. With the advent of multi-slice CT and its on-going refinement, isotropic sub-millimeter voxels can be obtained for the majority of clinical examinations. This has improved the diagnostic quality of image post-processing such that it has become a vital component of medical imaging today, in particular for CT angiography (Prokop 1997, Rankin 1999, Addis 2001). The axial source images contain the basic information of a CT scan. They can be supplemented by basic 3D post-processing tools and advanced methods for the analysis of complex anatomy, automated quantification, and functional evaluation (Vogl 2002, van Ooijen 2003, de Feyter 2005).

6.1 Trans-axial Image Slices

Trans-axial image slices are the basic outcome of a multi-slice CT scan and include all of the acquired information. In cardiac CT examinations, axial images should be reviewed in all cases, e. g., by scrolling through them up and down in the craniocaudal direction, which gives a quick overview of the relevant cardiac structures, including the coronary arteries. The matrix size for axial images in CT is generally 512 × 512 picture elements (pixels). Considered as a part of a 3D image volume, an axial image is a layer of 512 × 512 voxels within that volume. The size of the voxel in the image plane (x-y direction) is determined by the in-plane pixel size and therefore by the reconstructed field-of-view (FOV). The size of the voxel in the longitudinal direction (z-direction) is given by the slice width and the image increment. The FOV of an axial image is the diameter of the area that is depicted in the image. The in-plane voxel size can be calculated as FOV divided by matrix size. Typically, a FOV of 150–180 mm is chosen for image reconstruction in cardiac CT imaging, resulting in 0.29- to 0.35-mm in-plane voxel size. The in-plane voxel size is frequently misinterpreted as the in-plane resolution of a CT image. Instead, image resolution is mainly determined by the CT system geometry, detector aperture, and convolution kernel

(filter) chosen for image reconstruction. Only in rare cases does the in-plane resolution correspond to the in-plane voxel size. Typical CT scanner geometries and convolution kernels used for cardiac CT examinations provide a resolution of 8–12 lp/cm, which corresponds to an object size of 0.4–0.6 mm that can be differentiated. The resolution in the image is determined by the geometry of the scanner and not by the voxel size. Given the 512 × 512 pixels in the image, a 150- to 180-mm FOV produces an in-plane voxel size of 0.29- to 0.35-mm. However, the image resolution remains to be 0.4–0.6 mm, depending on the scanner and filter kernel parameters. Further reducing the FOV for image reconstruction will therefore reduce the in-plane voxel size, but will not increase image resolution. Only in special cases, such as high-resolution thorax imaging with a large FOV of 350–400 mm, will the in-plane voxel size be the limiting factor for in-plane resolution. As an example of visualization of the cardiac anatomy in axial slices, Fig. 6.1 shows axial images, acquired using a 64-slice CT scanner, at different anatomical

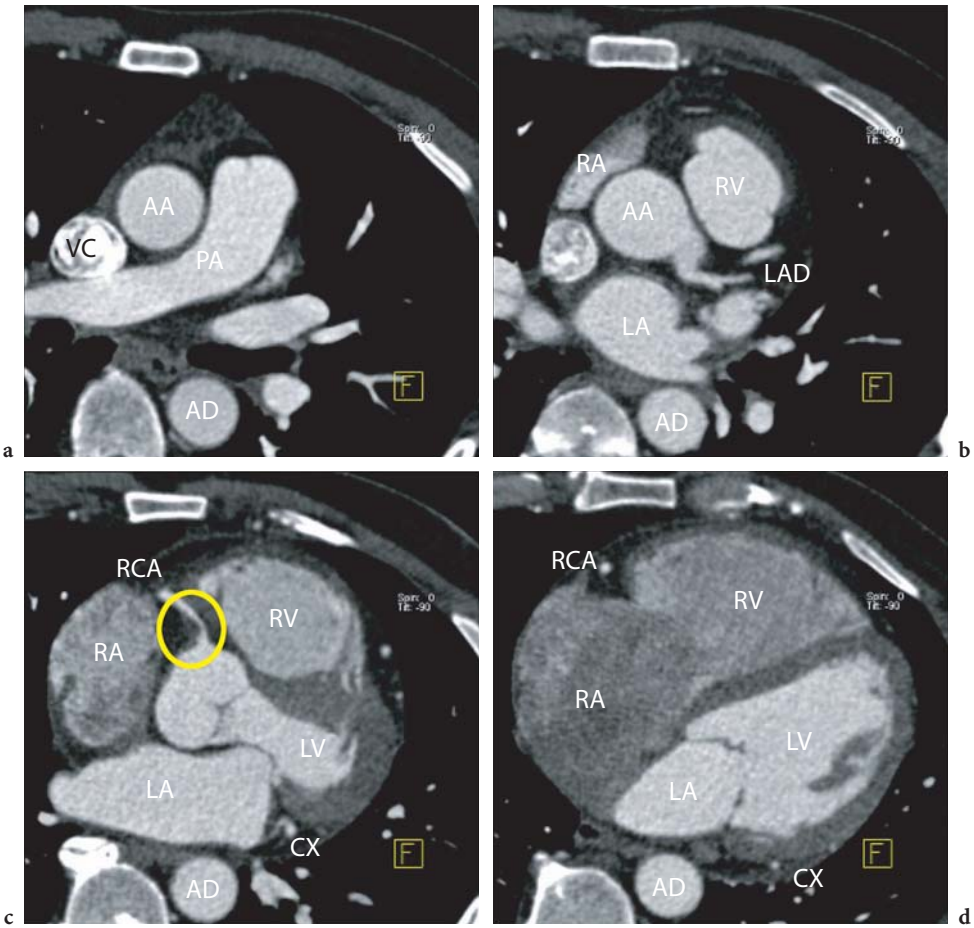

Fig. 6.1. Axial images at different anatomical levels (**a–d**, in craniocaudal direction) of a coronary CT angiography examination in a patient with a stenosis in the right coronary artery (*yellow circle*). The images were acquired using a 64-slice CT scanner with 64 × 0.6-mm slices per rotation and 0.75-mm slice width. Axial images include all of the information acquired in a CT scan and should be reviewed in any case, e.g., by scrolling through them. For better orientation, important anatomical landmarks have been labeled. *AA* Ascending aorta, *PA* pulmonary artery, *AD* descending aorta, *VC* vena cava, *RA* right atrium, *RV* right ventricle, *LA* left atrium, *LV* left ventricle, *LAD* left anterior descending coronary artery, *RCA* right coronary artery, *CX* circumflex artery. (Case courtesy of Erlangen University, Germany)

levels from a coronary CTA examination in a patient with a stenosis in the right coronary artery.

6.2 Multi-planar Reformation

In multi-planar reformations (MPRs), a plane is defined in a 3D image volume, and all voxels on that plane are visualized in a planar image. Simple examples of MPR orientations are sagittal and coronal views, which are widely used in general radiology but are of limited use in cardiac imaging due the complex course of the cardiac anatomy and the coronary arteries. Instead, oblique MPRs, which can be scrolled through similar to axial images, are the most helpful for cardiac CT. In this respect, two stacks of oblique planes are of particular interest: the planes parallel to a line along the left anterior descending artery (LAD), and the planes parallel to a line connecting the right coronary artery (RCA) and circumflex artery (CX) (Fig. 6.2). Scrolling through the first set of planes allows the tortuous course of the LAD to be followed, while scrolling through the second set of planes will display the anatomy of the RCA and CX.

MPR resolution depends on both the in-plane resolution of the original axial images and the through-plane resolution, which is a function of reconstruction slice width and image increment. For multi-slice spiral CT, through-plane resolution can be improved by reconstructing overlapping images with an increment that equals 50–70% of the reconstructed slice width. In this way, objects that are smaller than the reconstructed slicewidth can be resolved in the longitudinal (z-) direction. Depending on the orientation of the MPR, the relative influence of in-plane and longitudinal resolution varies, and so does the resulting MPR resolution for non-isotropic image data. Considering the typical in-plane resolution of about 0.5 mm for high-resolution cardiac CT angiography protocols, it is obvious that the reconstructed slice width of the axial source images should be as narrow as possible, at best sub-millimeter, to optimize MPR image quality. In general, the smallest available reconstruction slice width should be used as long as the signal-to-noise ratio of the images remains acceptable. For larger patients, the reconstruction of wider axial slices as an input for MPRs can be considered in order to find the best trade-off between image noise and longitudinal resolution. The latest generation of 64-slice CT systems can provide 0.4-mm longitudinal resolution using overlapping images with a reconstruction slice-width of 0.6 mm (Flohr 2004). As these scanners provide true isotropic image data with sub-millimeter resolution, the resolution of MPRs is then homogeneous and independent of the orientation of the MPR image planes.

To trade-off between image resolution and image noise, the MPR slice thickness can be modified. In that case, all voxels within a given distance orthogonal to the MPR plane are averaged, and a so-called slab-MPR is created. Slab-MPRs, e. g., with a slab thickness of 2–5 mm, are useful to reduce image noise and to visualize larger parts of tortuous cardiac anatomy.

Correct positioning of the MPR planes is critical for a correct diagnosis, as partial-volume effects may influence the assessment of anatomical details (Fig. 6.3). For this reason, multiple MPR stacks with different orientations and with overlapping reconstruction increments are widely used. On some CT scanners, pre-determined stacks of double-oblique MPRs along preferred planes can be directly reconstructed from the raw data to facilitate the clinical workflow (Fig. 6.4).

Alternatively, curved MPRs can be used that are defined on curved planes instead of straight planes and that capture the course of tortuous vessels and coronary arteries along their entire lengths in a single image (Fig. 6.5). To generate a curved MPR, the user interactively places multiple markers in the vessel of interest along its course while scrolling through the axial slices. The processing software then connects the markers with a fitted line and generates a MPR along this line. Newer evaluation software tools also provide an automated calculation of the centerline of the target vessel, which defines the curved visualization plane (see Sect. 6.5).

Curved MPR is particularly useful for displaying the in-stent lumen, as with this approach interference with the desired lumen information by the very dense stent material can be minimized (Fig. 6.6).

MPR techniques are readily and easily available and represent a standard feature on any basic 3D application package. MPRs do not require extensive

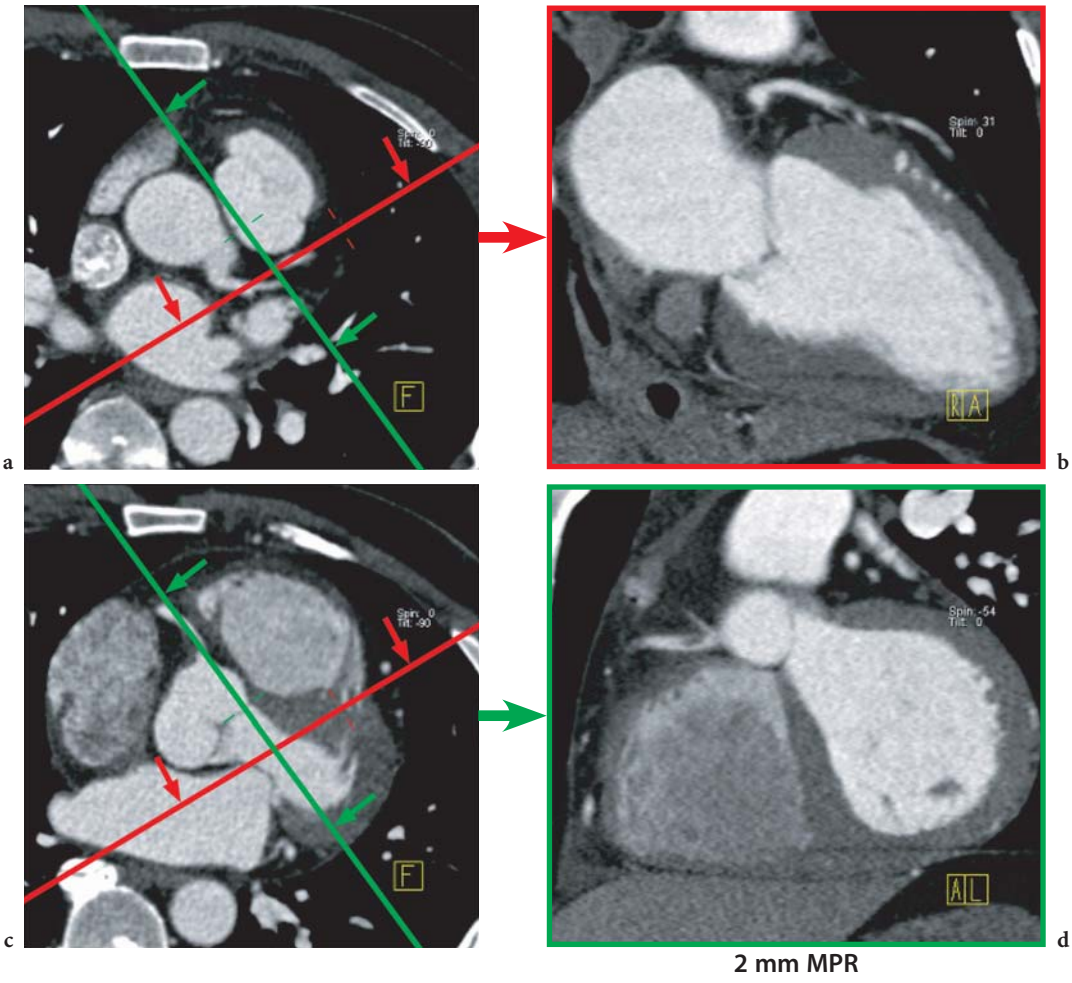

Fig. 6.2. Multiplanar reconstructions (MPRs) for a coronary CT angiography examination displaying the proximal *LAD* (**a**, **b**) and proximal *RCA* (**c**, **d**). The axial images were acquired using a 64-slice CT scanner with 64 × 0.6-mm slices per rotation and 0.75-mm slice width. MPR thickness was chosen to be 2 mm. The green and red lines in the axial images indicate the image planes of the MPRs. Stacks of MPRs in pre-defined directions are the basis for a standardized, routine evaluation of workflow. (Case courtesy of Erlangen University, Germany)

user interaction, such as the time-consuming manual segmentation of potentially overlapping structures that is needed in other post-processing approaches. Thus, MPRs are frequently used in routine clinical evaluation algorithms. They maintain the full information of the axial CT images, in particular the CT density values (HU values). However, since MPRs are operator-dependent, improper positioning of the MPR planes may introduce false-negative and false-positive stenoses, or incorrectly estimate the degree of stenoses. Interactive viewing of stacks of MPRs from multiple viewing angles combined with the use of curved MPRs is therefore recommended.

6.3 Maximum-Intensity Projection

Maximum intensity projections (MIPs) are arbitrarily oriented planar images similar to MPRs.

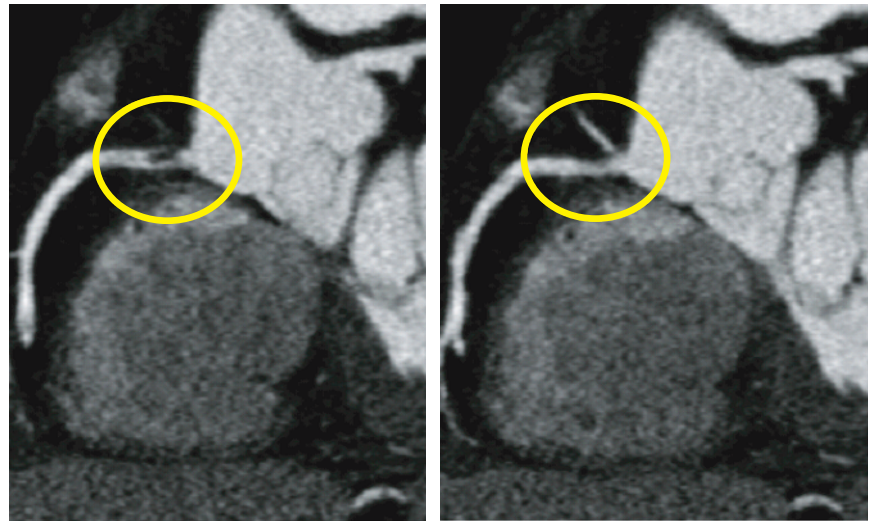

a b

Fig. 6.3a, b. Two MPRs on slightly shifted image planes along the RCA. While one MPR reveals a high-grade stenosis (**a**) the other has slightly shifted plane and reveals only a moderate stenosis (**b**) in the RCA (*yellow circles*). Positioning of the MPR planes is operator-dependent and improper positioning may introduce false-negative and false-positive stenoses or varyingly estimate the degree of stenoses. The use of MPRs from different viewing angles is therefore recommended. (Case courtesy of Erlangen University, Germany)

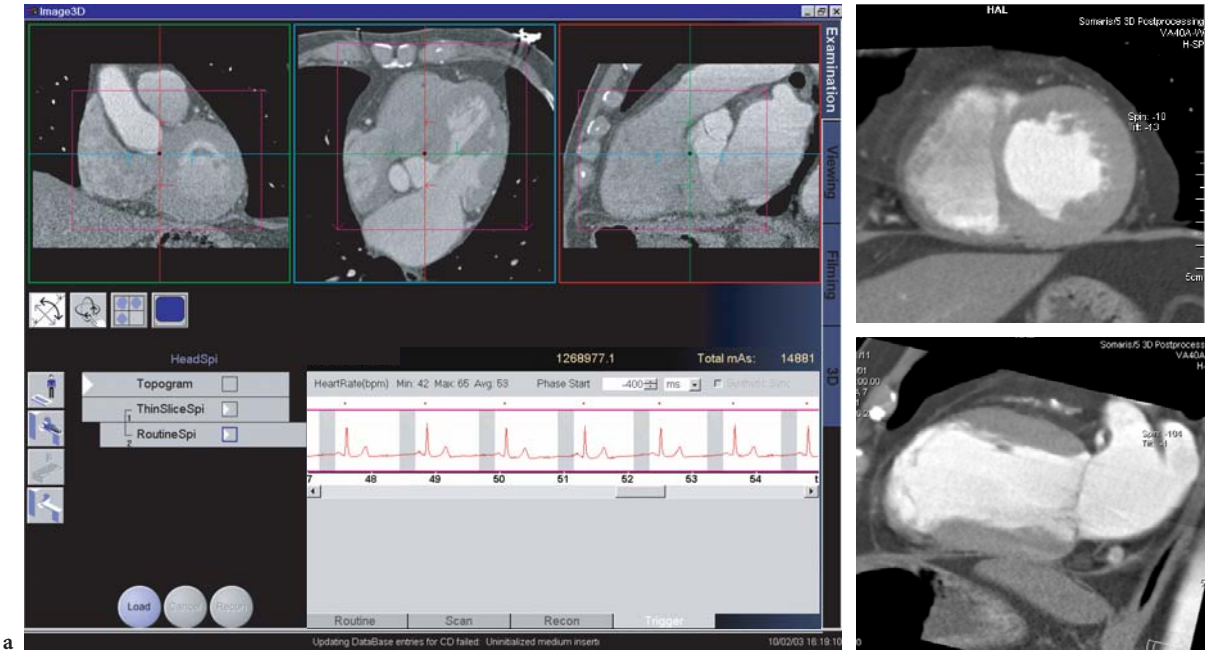

a b c

Fig. 6.4a–c. Direct MPR reconstruction for a cardiac CT examination obtained on a 16-slice CT scanner. True 3D-based planning of the MPR views (**a**) enables direct reconstruction of MPR stacks from the scan data with pre-defined MPR thickness and increment. The usual step of generating axial slices can be skipped. In the example given, MPR stacks in short (**b**) and long heart (**c**) axes are generated in diastolic phase. (Case courtesy of Tübingen University, Germany)

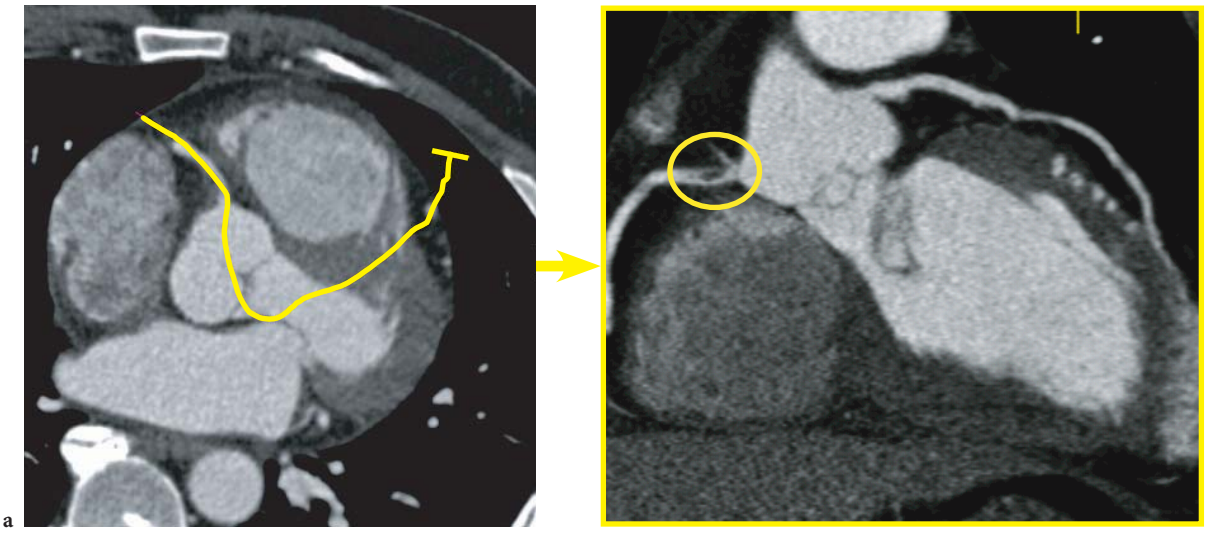

Fig. 6.5. Curved MPR for a coronary artery examination obtained on a 64-slice CT scanner. **a** The yellow line in the axial image indicates the curved image plane of the MPR, which has been generated manually by the user, with interactive placement markers in the vessel based on the axial slices. **b** The curved MPRs can be used to follow the course of a tortuous coronary artery along its entire length and reveals a high-grade stenosis in the proximal RCA (*yellow circle*). (Case courtesy of Erlangen University, Germany)

Each pixel of the 2D MIP image is generated from parallel rays that are cast through the 3D image volume. As result of the projection, the pixels in the MIP image represent the maximum CT number encountered in each ray. MIPs preserve the gray scale of the original axial images, and they reduce the visually perceived image noise without compromising the visually perceived image sharpness. The differentiation between contrast-enhanced vascular structures and background is good, and calcifications can be clearly depicted. However, MIPs do not provide any depth information, which is a drawback for the visualization of complex anatomy, such as the thoracic vessels, but does not play a major role for coronary artery imaging. MIPs are projection images, and thus high-density structures such as the contrast-filled cavities of the heart may overlap the coronary arteries in the projection direction and obscure structures of interest. For the same reason, hypo-attenuating intraluminal lesions may not be identified, unless they are adjacent to the vessel wall and the proper viewing direction has been chosen.

To avoid these shortcomings, thin-slab MIPs (Rubin 1993) have been introduced. These are obtained by first generating thin-slab MPRs from which the MIP images are reconstructed. In a thin-slab MIP, the maximum CT number within a given distance orthogonal to the MIP plane is displayed for every ray. For an evaluation of coronary arteries, the thickness of the slab has to be adjusted to the size and the course of the artery. Typical slab thicknesses range from 3 to 10 mm. In a standardized approach, the reconstruction of overlapping thin-slab MIP images with an increment smaller than the slab thickness (e.g., 1-mm increment for a 3-mm slab thickness) is recommended.

For visualization of cardiac and coronary anatomy, the same planes as discussed for slab MPRs should be considered (see Sect. 6.2). In particular, for diagnosis of the coronary arteries, planes in parallel to a line connecting RCA and CX, and planes in parallel to a line along the LAD should be used. MIPs with 5-mm thickness along the RCA and LAD are shown in Fig. 6.7, and can be directly compared to the corresponding MPR reconstructions that have been generated in identical planes (Fig. 6.2).

In a more interactive evaluation approach, thin-slab MIPs can be scrolled through the volume (sliding thin-slab MIPs). By carefully adjusting both the thickness and the orientation of the MIP plane, each

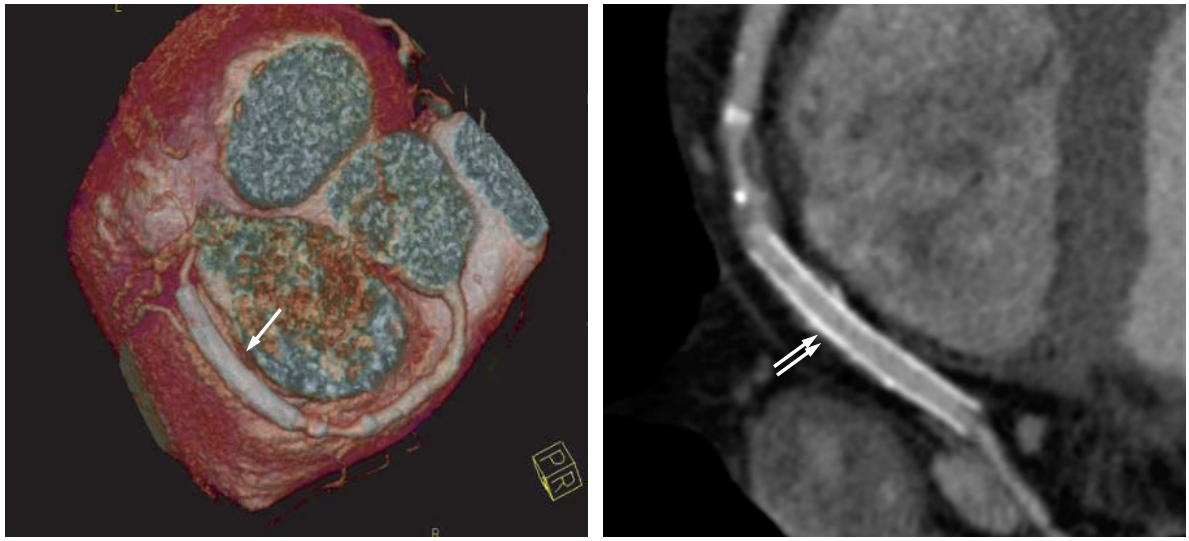

a b

Fig. 6.6a, b. Curved MPR for a coronary artery examination obtained on a 16-slice CT scanner with 16 × 0.75-mm collimation. The patent in-stent lumen of the stent in the distal RCA coronary artery can be demonstrated in VRT display (**a**, *arrow*) and is readily visualized with curved MPR reconstruction (**b**, *double arrow*). (Case courtesy of HSC Medical Center, Kuala Lumpur, Malaysia)

coronary artery can be displayed in its entire length in many cases. Similar to the automated generation of pre-defined MPR stacks, some CT scanners allow for reconstruction of pre-determined stacks of double-oblique MIPs along preferred planes directly from the raw data, thus facilitating the clinical workflow (Fig. 6.8).

More recent software platforms allow for the reconstruction of curved MIPs in analogy to curved MPRs (Raman 2003). In analogy to curved MPRs, curved MIPs are generated by the interactive placement of multiple markers in the vessel of interest along its course while scrolling through the axial slices. The processing software then connects the markers with a fitted line and generates a MIP along this line. Newer evaluation-software tools also provide an automated calculation of the centerline of the target vessel that defines the curved visualization plane (see Sect. 6.5). Some illustrative examples of in which curved MIPs are directly compared with curved MPRs in identical planes are shown in Fig. 6.9.

Similar to MPRs, MIPs are fast and readily available, and they are included in any basic 3D evaluation-software platform. In many institutions, MIPs are the basis for a standardized routine evaluation workflow. When the slab thickness is properly selected, visualization of non-calcified and mixed plaques is excellent (Fig. 6.10). However, MIPs use only a part of the available data, thus discarding information that is included in the original axial images. Relevant anatomical details may be obscured by overlapping structures, and stenoses may be under- or overestimated (van Ooijen 2003). MIPs are not recommended for the visualization of stents or heavily calcified coronary vessels, since the vessel lumen will be obscured due to the principle of the MIP projection (Fig. 6.10).

6.4 Volume-Rendering Technique

Direct volume-rendering techniques (VRTs) are advanced 3D post-processing methods that have meanwhile entered clinical routine due to continuous improvement in computer hardware and software. VRTs use all available data in the volume image. A

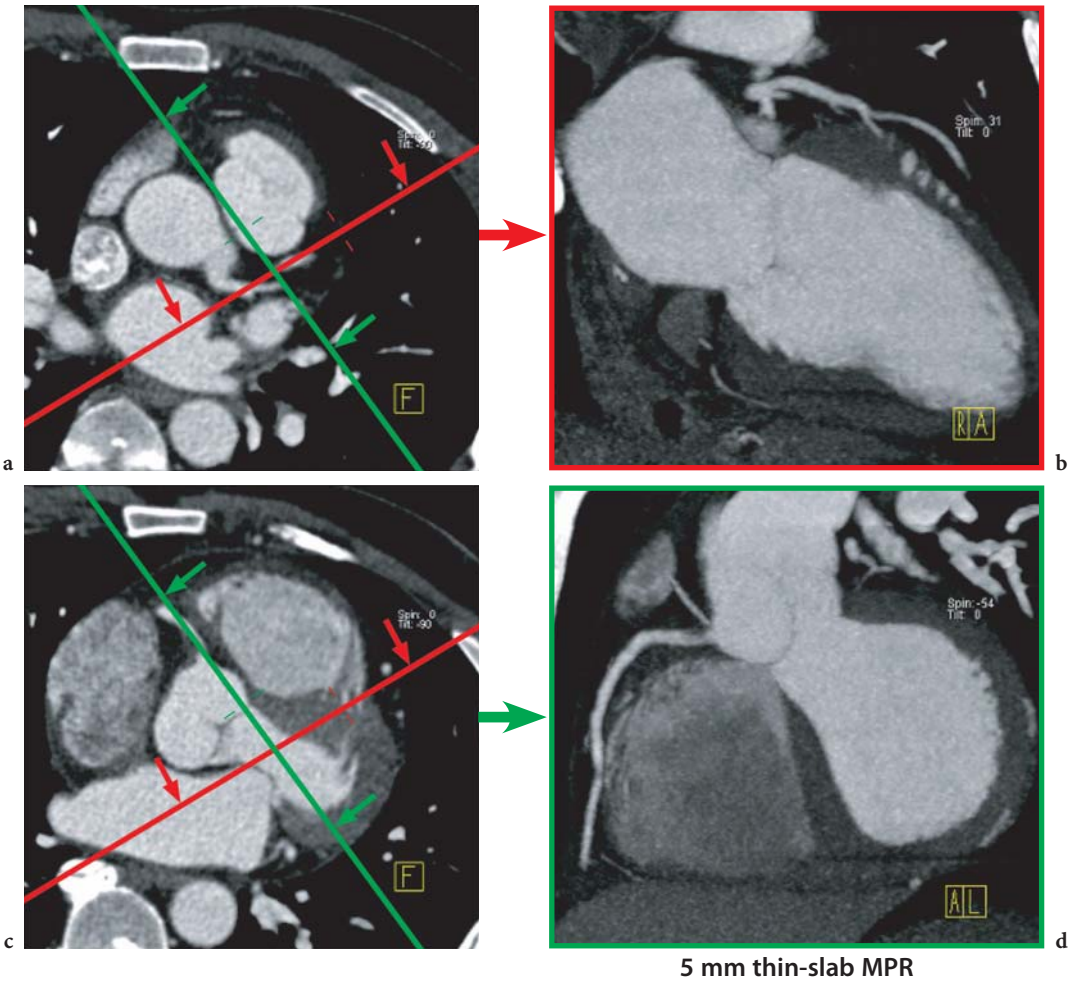

Fig. 6.7. Maximum-intensity projection (MIP) for a coronary CT angiography examination displaying the proximal LAD (**a**, **b**) and proximal RCA (**c**, **d**). The axial images were acquired using a 64-slice CT scanner with 64 × 0.6-mm slices per rotation and 0.75-mm slice width. MIP slab thickness was chosen to be 5 mm. The green and red lines in the axial images indicate the image planes of the MIPs. (Case courtesy of Erlangen University, Germany)

voxel-intensity histogram is generated, and several parameters, such as color, brightness and opacity, are assigned to each voxel according to its HU value. Similar to MIP projections, rays are cast through the 3D image volume. Unlike MIPs, however, all voxels along a ray contribute to the resulting pixel in the VRT image proportional to their opacities.

The opacities of all voxels are summed up using weighting factors. Assume walking along a ray through the object from voxel 1 to voxel (n – 1) and finally voxel n. The CT density Sum_n of the resulting pixel in the VRT image can be calculated according to the recursive equation (Eq. 6.1).

$$Sum_n = Op_n \cdot CT_n + (1 - Op_n) \cdot Sum_{n-1} \qquad (6.1)$$

Opn is the opacity of voxel n and CT_n is its HU value. An opacity of 0 ($Op_n = 0$) means that the corresponding voxel is completely transparent; it does not contribute to the resulting VRT image. An opacity of 1 ($Op_n = 1$) means that the corresponding voxel is completely opaque. Values between 0 and 1 charac-

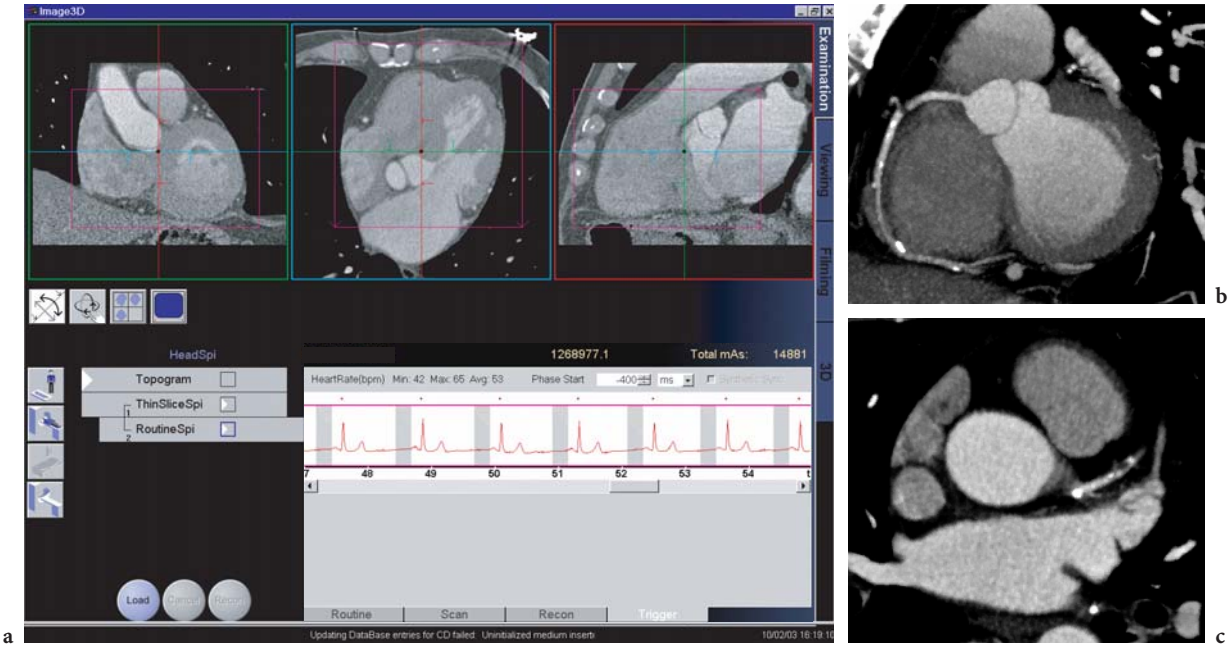

Fig. 6.8a–c. Direct MIP reconstruction for a cardiac CT examination obtained on a 16-slice CT scanner. True 3D-based planning of the MIP views (**a**) enables direct reconstruction of MIP stacks from the scan data with pre-defined MIP slab thickness and increment. The usual step of generating axial slices can be skipped. In the example, the MIP stacks are generated in diastolic phase using RAO (**b**) and LAO (**c**) projections. (Case courtesy of Tübingen University, Germany)

terize different degrees of transparency. It is obvious from Eq. 6.1 that when a pixel n with opacity $Op_n = 1$ is traversed, the contribution of all preceding voxels will be set to 0, since the term $(1 - Op_n)$ then equals 0. In other words, as soon as a completely opaque voxel has been traversed, only this voxel will be shown in the resulting image and all previously traversed voxels will be hidden. Assigning different opacities to different ranges of CT values enables the user to control the contribution of voxels within these CT density ranges to the resulting VRT image. The user can make these voxels more or less transparent, thus hiding or showing the corresponding anatomical details and adjusting the 3D depth, contrast, and transparency of the VRT image. The relevant anatomical structures in cardiac images are fat, with a CT density of approximately – 100 HU; soft tissue, with a CT density of approximately 50 HU; contrast-filled vessels, with a CT density of approximately 200–300 HU, and calcifications and bony structures with a CT density > 100–150 HU. Usually, linear, triangular, or trapezoidal functions are used to assign opacity to a certain CT density range. Figure 6.11 shows a gray-scale VRT reconstruction of a heart. At the bottom, the histogram of the CT values is shown together with the opacity curve. The opacity for all voxels with a CT density less than – 80 HU is set to zero and these voxels are not displayed in the resulting VRT. The opacity increases linearly in the range – 80 HU to 250 HU; constant maximum opacity is assigned to all voxels with a CT density > 250 HU. With these settings, soft tissue is relatively transparent and contrast filled vessels – the structures of interest – are relatively opaque. The visibility of the contrast filled coronary arteries is therefore enhanced. Figure 6.11 also demonstrates the effect of increasing maximum opacity levels.

Instead of gray values, colors can be attributed to the voxels according to their CT numbers (Fig. 6.12). Although the choice of colors is arbitrary, brownish red is most commonly used for soft tissue in the heart. To improve the visibility of boundaries between different tissue types and the delineation of anatomical structures, gradient transfer functions are used in more elaborate VRT approaches. For

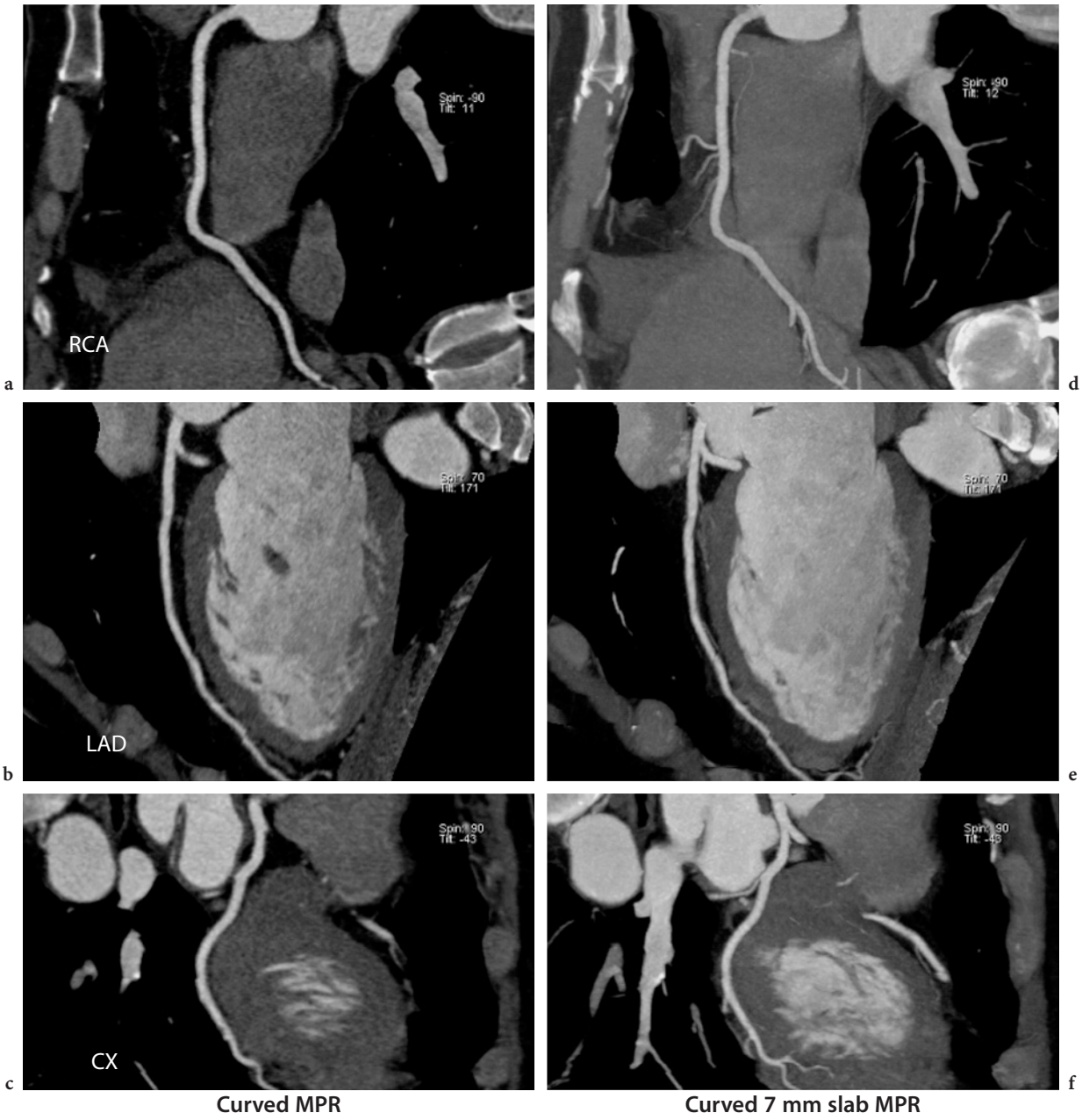

Fig. 6.9. Curved MPRs (**a–c**) and curved thin-slab MIPs (**d–f**) along the LAD, RCA and CX in a patient with normal coronary anatomy. The curved MPR was generated with 2-mm MPR thickness; for the curved MIP, the MIP slab thickness was 7 mm. The images were generated based on an automatically detected centerline of the vessels, which defines the curved visualization plane. The direct comparison shows that curved MIP provides a more detailed view of the coronary anatomy than curved MPR. (Case courtesy of Erlangen University, Germany)

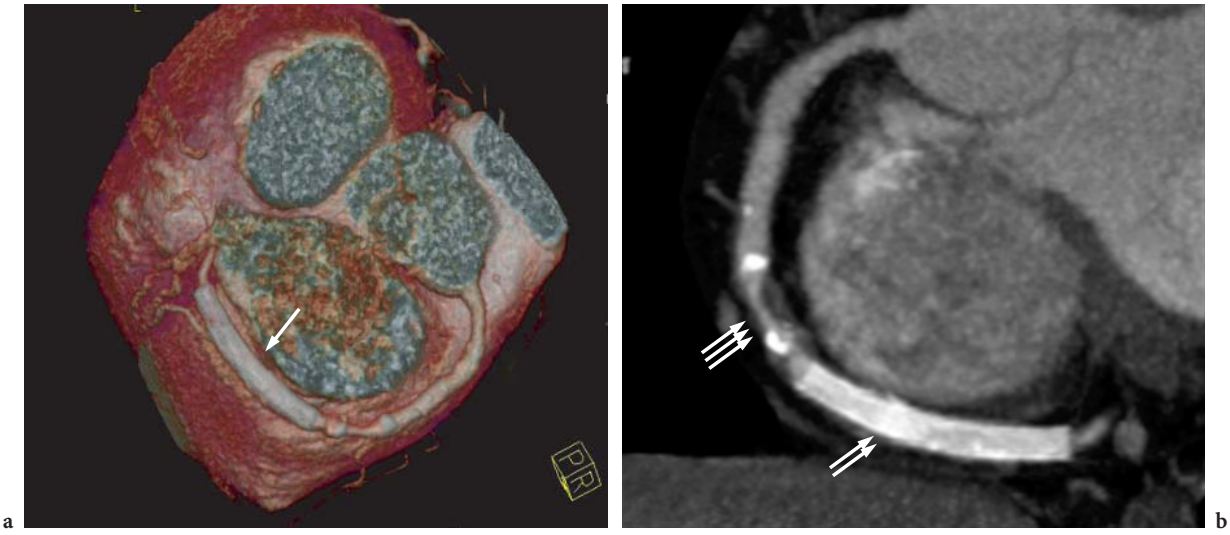

Fig. 6.10a, b. Manually defined curved MIP with 5-mm slab thickness for a coronary artery examination obtained on a 16-slice CT scanner with 16 × 0.75-mm collimation. The in-stent lumen of the stent in the distal RCA can be demonstrated in VRT display (**a**, *arrow*) and cannot be adequately visualized with curved MIP reconstruction (**b**, *double arrow*). Therefore, MPR is to be preferred over MIP for the visualization of in-stent lumen. However, visualization of the stenotic lesion and the corresponding mixed plaque (**b**, *triple arrow*) is excellent. (Case courtesy of HSC Medical Center, Kuala Lumpur, Malaysia)

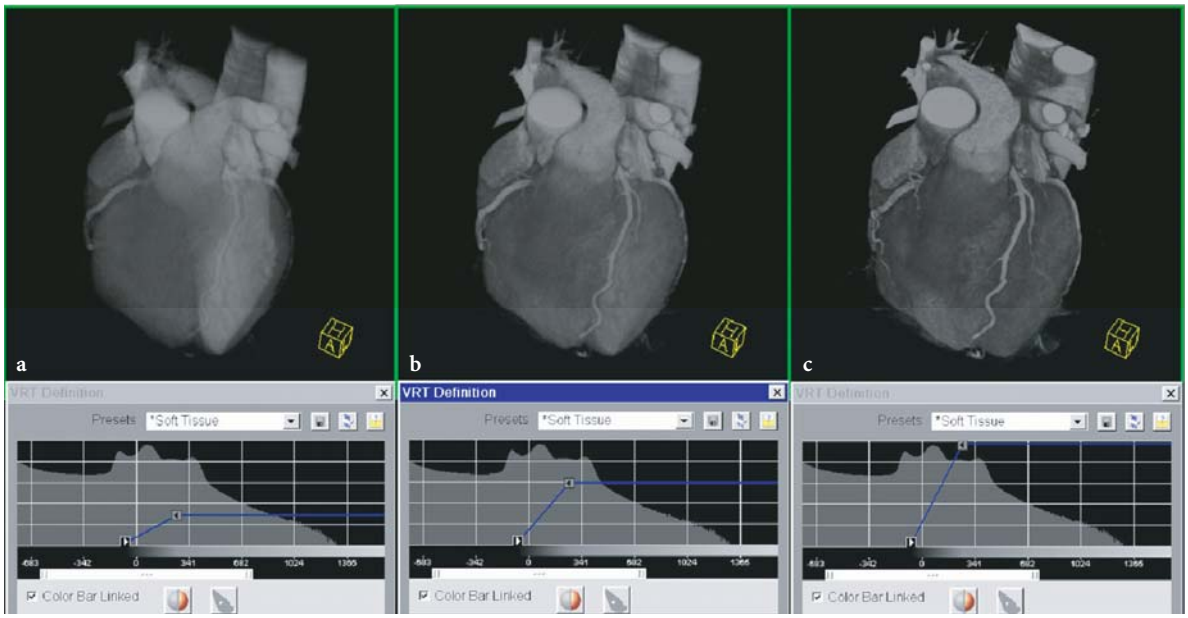

Fig. 6.11a–c. Volume-rendering images (VRTs) demonstrating the influence of opacity. An opacity value is assigned to each voxel according to its CT number, in order to make the voxel more or less transparent. The diagrams on the bottom indicate the histogram of the CT values and the respective opacity functions (*blue lines*). **a** When using low overall opacity the image looks transparent and has a large 3D depth but it lacks contrast. LAD and CX are hardly visible. **b** For medium overall opacity, the 3D depth decreases and contrast increases. **c** With high overall opacity, only the surface of the heart is visible, but the coronary arteries are much better and sharper delineated

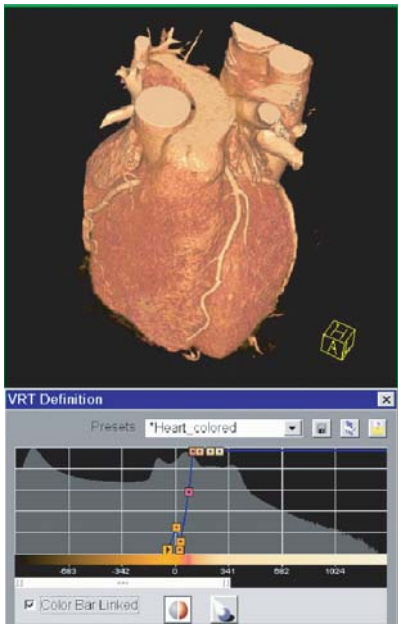

Fig. 6.12. In a VRT, colors instead of gray values can be attributed to the voxels according to their CT numbers. In this example, soft tissue is assigned a brownish red, whereas a lighter brown is used for the contrast-filled coronary arteries with higher CT numbers

this purpose, the opacity is modulated according to the local CT density gradients. In homogenous areas with small density changes (small gradients), the opacity is reduced; these areas will therefore be visualized more transparently. In areas with abrupt density changes, the opacity is increased. Furthermore, shading can be used to improve the 3D impression of the images.

VRTs require extensive user interaction for adequate imaging results. In many cases, the segmentation of overlapping structures is required, e.g., to remove the rib cage and the pulmonary vessels for a VRT visualization of the heart. Common approaches are the use of clip planes and volume of interest "punching". Alternativley, slab VRTs can be used for an interactive evaluation of anatomical details that are defined similar to slab-MPRs and slab-MIPs. With more recent and advanced cardiac evaluation packages, the heart can be automatically isolated and VRT display of the cardiac and coronary anatomy becomes feasible without further segmentation.

VRTs depend on a multitude of user-definable parameters. They are helpful for visualization of diagnostic results, in particular to referring physicians, but they are of limited use for primary diagnosis in cardiac CT examinations. The variety of parameters and settings and the lack of standardization impair the ability of VRTs to correctly assess coronary diameters and coronary artery stenoses (Mahnken 2003). However, VRTs provide good insight into the 3D relationship of anatomical structures and thus are helpful in the evaluation of aberrant coronary anatomy, such as anomalous coronary arteries, and bypass grafts (Fig. 6.13).

There are other 3D post-processing techniques related to VRT that can be used for cardiac CT, such as virtual endoscopy, which is known from CT colonography. Virtual endoscopy can provide spectacular visualization of the inner surface of contrast-filled coronary arteries (Fig. 6.14), but its clinical use in cardiac imaging remains to be shown.

6.5 Vessel Segmentation and Vessel Analysis

Recently, advanced vessel segmentation and vessel analysis tools have been introduced that provide the user with an optimized clinical workflow for assessing the lumen of coronary arteries, identifying and quantitating stenoses, evaluating the coronary wall, and investigating coronary stents. These advanced application packages make use of all available 3D post-processing techniques, such as MPRs, MIPs and VRTs, and combine and modify them with the goal of simplifying and streamlining the clinical workflow. In addition to these tools, detailed reporting functionality, e.g., based on DICOM-structured reporting, is an essential requirement for advanced cardiac and coronary analysis packages in order to integrate them into routine clinical workflow.

Advanced analysis packages typically show MPRs and a VRT of the cardiac image data set for a preliminary orientation, with the rib cage automatically removed so that only the relevant structures of the heart and the great vessels are displayed in the VRT image. Vessels can then be automatically segmented

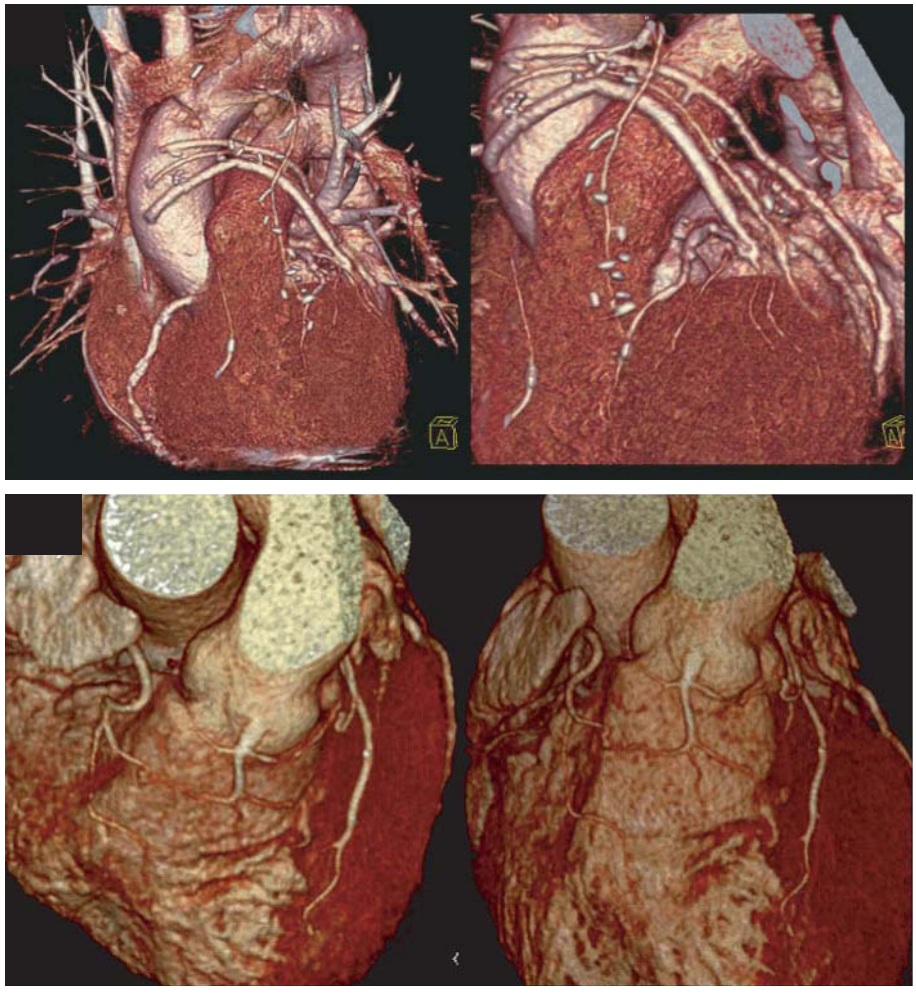

a

b

Fig. 6.13a, b. VRTs are mainly useful for a demonstration of the diagnosis. They provide good insight into the 3D relationship of anatomical structures, e.g., in the case of anomalous coronary arteries or bypass grafts. The two cases given as examples were obtained on a 64-slice CT scanner with 64 × 0.6-mm slices per rotation. **a** In one patient, four bypass grafts canbe accurately be localized using VRT. **b** In another patient, the VRT display reveals an anomalous coronary artery originating from the pulmonary trunk. (Cases courtesy of Medical University of South Carolina, USA)

to calculate curved MPRs or curved MIPs along the respective center lines. Two different types of vessel segmentation are currently used. In the "vessel probe" approach, a marker is placed with a mouse click in the vessel of interest, either in the MPRs or in the VRT representation. A centerline extending on both sides of the marker is calculated, and the corresponding vessel segment is displayed as a curved MPR. Vessel probe approaches are fast and intuitive. As a drawback, the length of the displayed vessel segment cannot always be controlled, as it often depends on the quality of the image data set, and side branches of the vessel cannot be traced in the same evaluation. In the "vessel segmentation" approach, the entire coronary artery tree is segmented as a first step. If certain arteries or branches are not initially recognized by the segmentation algorithm, they can usually be appended to the coronary tree by

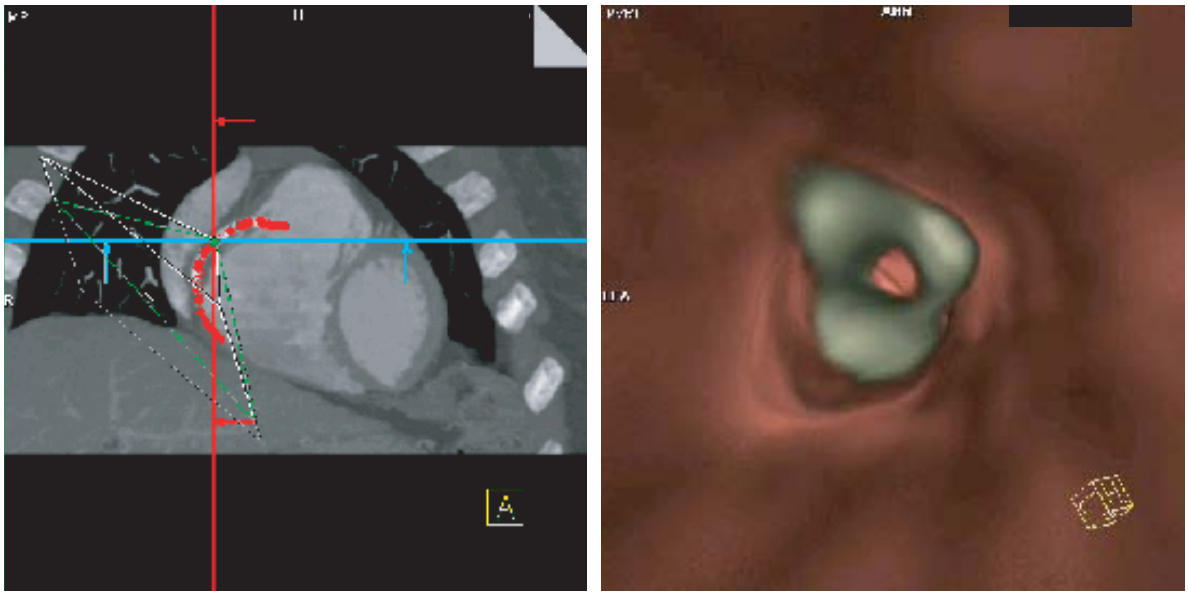

a b

Fig. 6.14a, b. Virtual endoscopic view with VRT visualization of a RCA based on an examination obtained on a 16-slice CT scanner with 16 × 0.75-mm collimation. **a** A path is being planned through the RCA that includes a stent. **b** The coronary artery lumen and stent struts can be visualized with virtual endoscopy. (Case courtesy of Mt. Sinai School of Medicine, New York, USA)

marking them with an additional mouse click. The isolated coronary tree is then displayed as a VRT image (Fig. 6.15), and the user can define centerlines between two arbitrary points on that tree as a basis for displaying the respective arteries or segments as curved MPRs or curved MIPs. Ideally, these curved MPRs (or curved MIPs) can be freely rotated to allow the inspection of plaques or stenoses from different viewing angles. MPRs on straight planes perpendicular to the centerline of the vessel are shown in addition to the curved MPR to facilitate the comprehensive evaluation of coronary stenoses, including calcified, fibrous, and lipid rich plaques. In some of these advanced application packages, the degree of a stenosis has to be manually measured (e.g., by a length measurement using an electronic ruler). In others, the degree of stenosis can be automatically determined by calculating area ratios of the vessel's cross-sections. As a representative example, Fig. 6.16 shows a screenshot of a comprehensive cardiac evaluation tool (syngo Circulation, Siemens, Forchheim, Germany) that provides automated segmentation of the coronary artery tree and subsequent measurement of stenosis.

As discussed in Sects. 6.2 and 6.3, curved MPRs and curved MIPs can be generated based on automatic calculation of the centerline of a segmented coronary artery that defines the curved visualization plane. Figures 6.17 and 6.18 demonstrate the feasibility of curved MPRs and curved MIPS with automated centerline detection in two patients with severe coronary artery disease. The cross-sectional images at the positions indicated by the markers are perpendicular to the vessel and allow for a detailed evaluation of plaques and wall changes, including density measurements.

In addition to vessel segmentation approaches, there is on-going development of advanced evaluation tools that help visualize and quantify plaques in the coronary arteries. Clinical studies have demonstrated the potential of multi-slice cardiac CT to not only detect but to some degree also characterize non-calcified and calcified plaques in the coronary arteries based on their CT attenuation (Schroeder 2001a, Schroeder 2001b, Leber 2004, Leber 2005). Figure 6.19 shows an example of a work-in-progress plaque evaluation tool with color-coding of voxels belonging to three different ranges of CT numbers

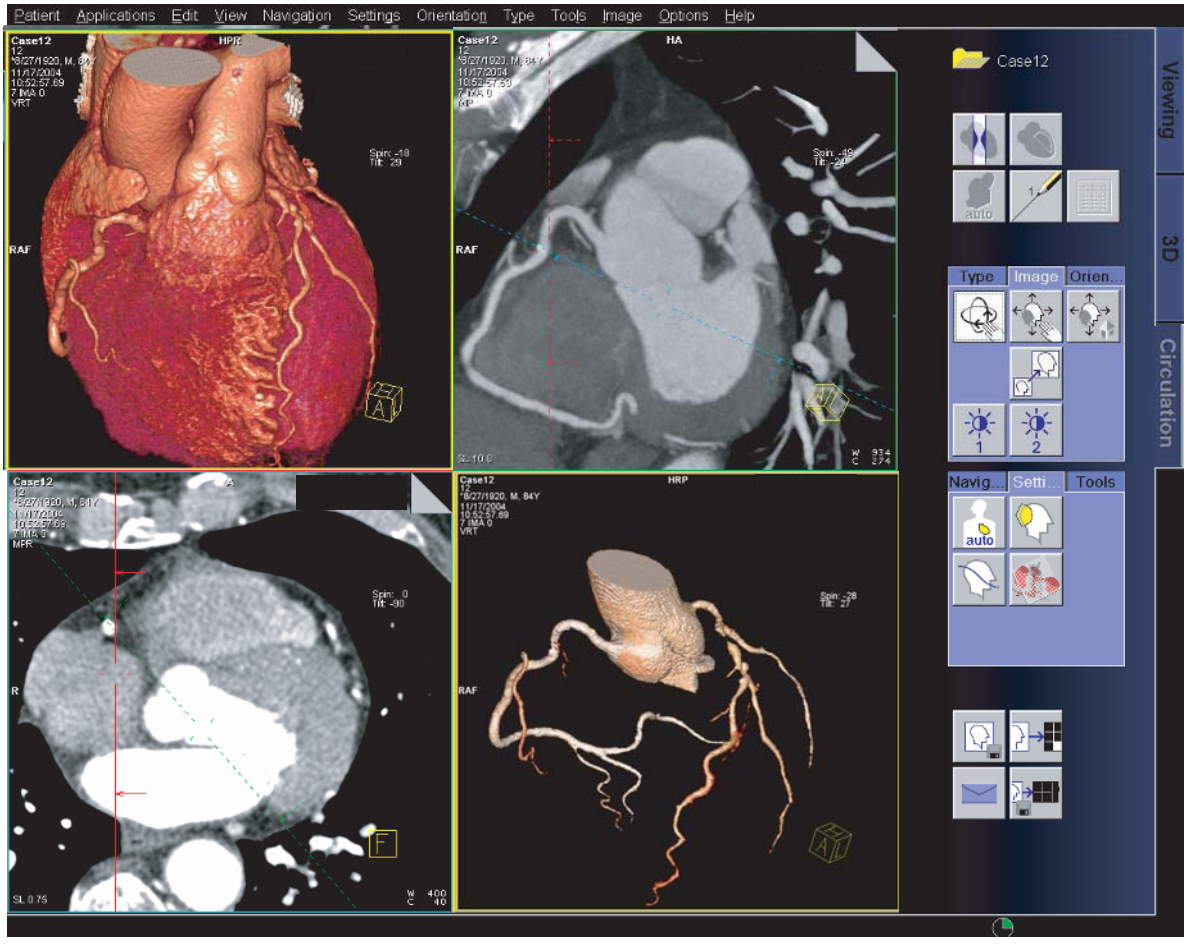

Fig. 6.15. An automated segmentation of the entire coronary artery tree, based on an examination obtained on a 64-slice CT scanner with acquisition of 64 × 0.6-mm slices per rotation. Based on the isolated heart with the rib cage removed (*upper left quadrant*), the software detects all coronary segments from a single marker (*lower right quadrant*) that was placed in the aorta just above the origin of the left main coronary arteries. (Case courtesy of Toyohashi Heart Center, Japan)

that may represent different types of plaques. The volume of the three compartments can be calculated, and an individual "plaque burden" can be derived for the patient. Clinical studies are needed to evaluate the potential and the clinical relevance of these plaque quantification tools. Ideally, they could, for example, be used to monitor the therapy response of patients undergoing medical treatment aimed at reducing their total plaque burden.

6.6 Four-Dimensional Visualization and Functional Parameter Assessment

Four-dimensional image data for the evaluation of functional parameters are readily available as an add-on for every retrospectively ECG-gated cardiac CT angiography examination. Compared to MR,

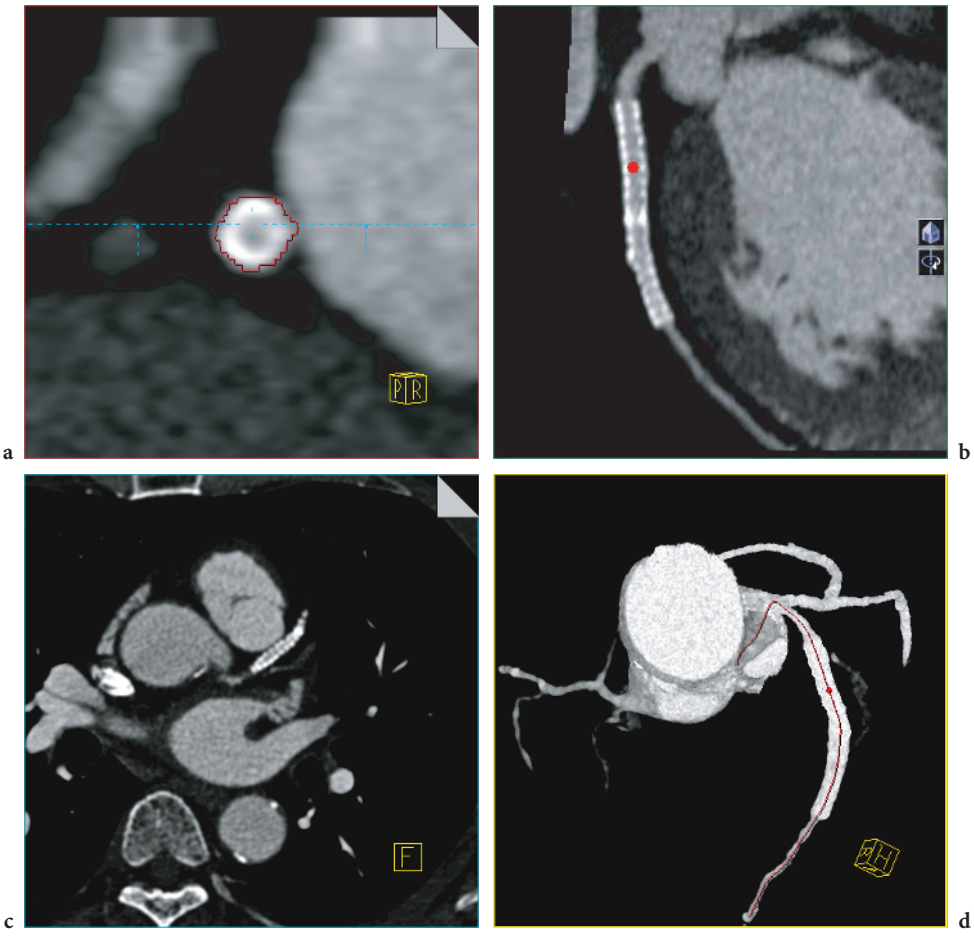

Fig. 6.16a–d. Example of a modern software-evaluation platform for automated segmentation and analysis of the coronary arteries based on an examination obtained on a 64-slice CT scanner with acquisition of 64 × 0.6-mm slices per rotation. **d** VRT visualization of the segmented coronary artery tree including the centerline (*indicated in red*) along the LAD is used for an overview. **b** An additional double-oblique MIP in the LAO helps to localize the exact position of the stent. **c** A curved MPR along the centerline allows for excellent visualization of the stent lumen due to isotropic sub-millimeter resolution. a A cross-section perpendicular to the centerline at the position indicated by the red marker allows for accurate measurement of the lumen. (Case courtesy of Erasmus University, Rotterdam, Netherlands)

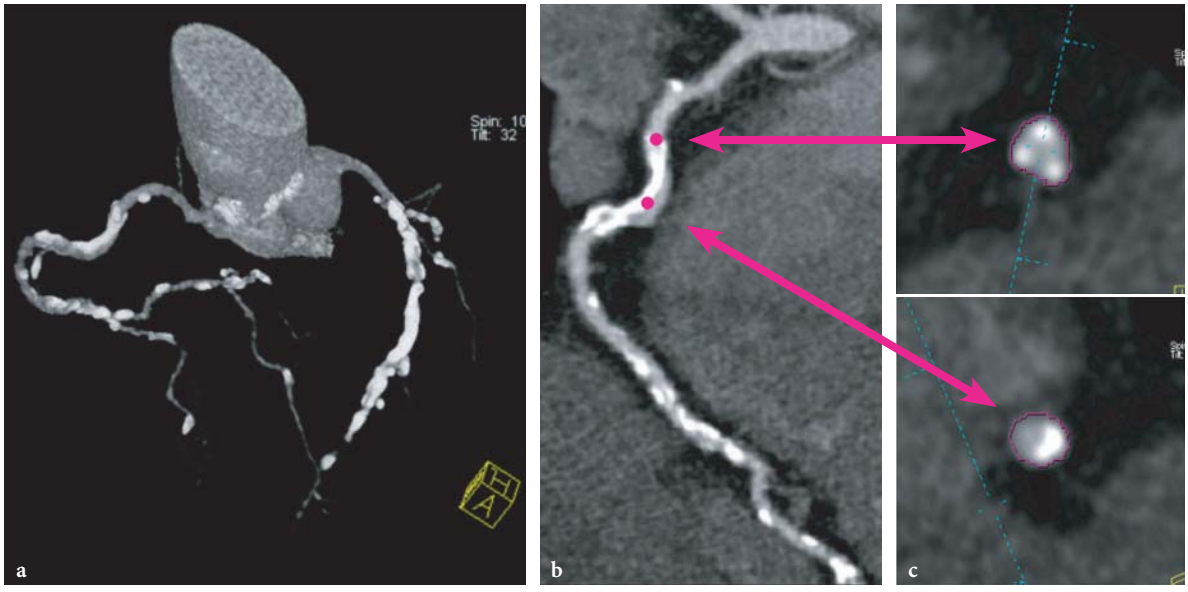

Fig. 6.17a–c. Automated coronary analysis for a patient examination obtained on a 64-slice CT scanner with acquisition of 64 × 0.6-mm slices per rotation. The software generates a the segmented coronary artery tree, **b** a curved MPR along the RCA, and c two cross-sections perpendicular to the centerline of the RCA for this patient with severe 3-vessel disease. The *pink dots* mark the positions of the cross-sectional images. (Case courtesy of New York University, USA)

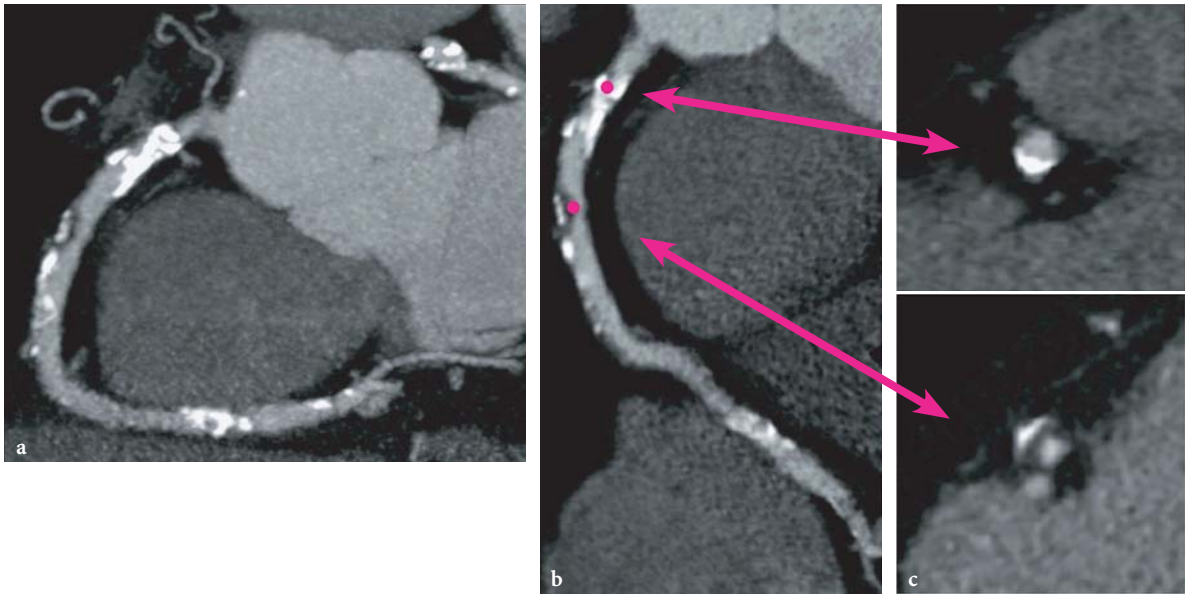

Fig. 6.18a–c. Automated coronary analysis for a patient examination obtained on a 64-slice CT scanner with acquisition of 64 × 0.6-mm slices per rotation. The software generates **a** a thin-slab curved MIP along the RCA and **b** a curved MPR along the RCA based on the detected center line and c two cross-sections perpendicular to the centerline of the RCA in this patient with severe 3-vessel disease. The *pink dots* mark the positions of the cross-sectional images. (Case courtesy of Mayo Clinic Rochester, Minnesota, USA)

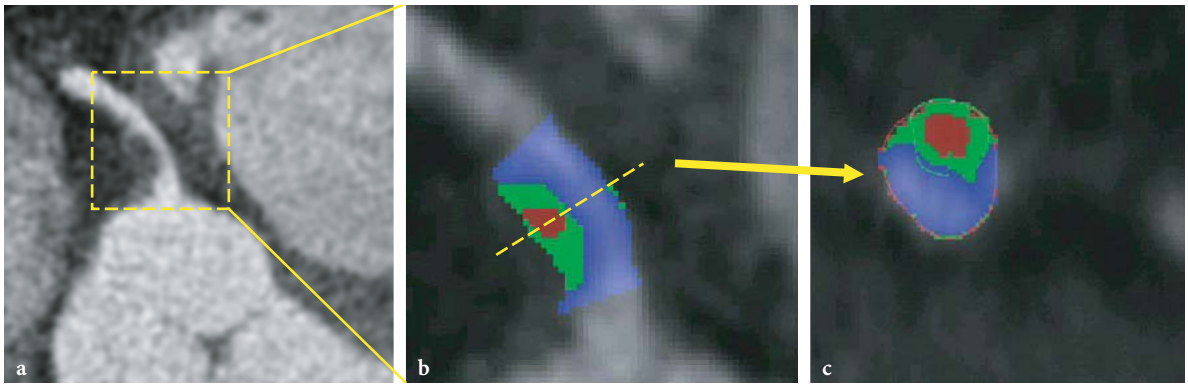

Fig. 6.19a–c. A work-in-progress plaque evaluation tool. Different colors are assigned to voxels within different ranges of CT numbers. **a** A MPR view reveals a significant stenotic lesion in the proximal RCA in this patient, who was scanned with a 64-slice CT scanner using 64 × 0.6-mm slices per rotation. **b** Color-coding can be applied to this MPR and **c** to **a** cross-sectional image perpendicular to the centerline cutting through the lesion. Red is used for voxels with CT numbers between –25 and 40 HU (potential "lipid" plaques), green for voxels with CT numbers between 40 and 110 HU (potential "fibrous" plaques), and blue for voxels with CT numbers between 110 and 445 HU (contrast-filled lumen). An additional threshold and color code can be defined for calcified plaques. (Case courtesy of Erlangen University, Germany)

multi-slice CT allows for a reliable assessment of left and right ventricular volumes, including left ventricular ejection fraction, and of regional wall motion at rest. Other parameters, such as peak filling rate, peak ejection rate, and regional wall motion under stress, cannot reliably be determined due to the still-limited temporal resolution of current multi-slice CT systems (Mahnken 2005a). Dedicated 4D visualization and evaluation tools are being developed to allow assessment of basic functional parameters from ECG-gated CT image data, such as end-systolic and end-diastolic volumes, stroke volume, ejection fraction, and myocardial mass. Advanced 4D visualization and quantification software also provides cine views of the beating heart and are generated from 3D data sets that were reconstructed at equidistant time points during the cardiac cycle. These tools can provide both visual and quantitative information regarding motion of the cardiac and coronary anatomy, ventricular wall motion, and ventricular wall thickening.

Series of complete 3D image data sets reconstructed in different phases of the cardiac cycle, at least in the end-systolic and end-diastolic phases (usually reconstructed with, respectively, 20 and 80% relative delay to the onset of the R-wave), are needed for functional evaluation. Some evaluation tools require input data in the form of double-oblique MPRs generated from the original axial slices along the short and long heart axess (Fig. 6.20). These MPRs can be reduced in their spatial resolution in order to limit the amount of data that has to be handled, e.g., by using 5- to 8-mm MPR thickness or a reduced 256 × 256 image matrix. The ability of some CT scanners to directly generate double-oblique MPRs along the short and long axes of the heart based on the raw scan data in different phases of the cardiac cycle (see Sect. 6.2) can simplify the clinical workflow. To derive functional parameters, such as ejection fraction and myocardial mass, endocardial and epicardial contours may have to be drawn manually for one slice position of the short axis view, followed by an automatic propagation to other slice positions between the base and the apex of the heart. Wall thickening is most commonly displayed in the form of a polar map based on short axis reformations, known as a "bulls-eye plot", following the AHA 17-segment classification.

More recent evaluation-software platforms require series of thin and overlapping axial slices in different phases of the cardiac cycle as an input for functional evaluation, similar to the input needed for cardiac anatomy and coronary artery analysis. A manual or automatic definition of the basal plane through the mitral valve, which separates the left ventricle from the left atrium, in both end-systole and end-diastole is generated, after which the blood pool in the left

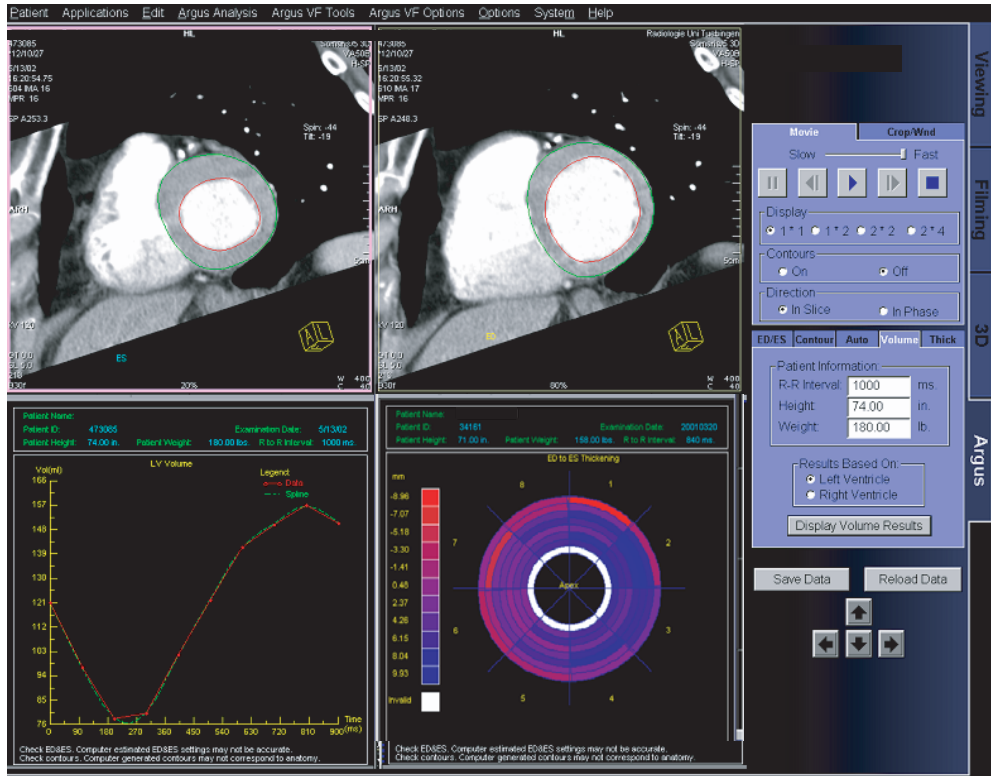

Fig. 6.20. CT examination of a patient with an occlusion of the left descending coronary artery using a 16-slice CT scanner with 16 × 0.75-mm collimation. Images for functional evaluation were reconstructed in 10 phases during the cardiac cycle, ranging from 0 to 90% of the RR-interval. The cardiac function evaluation software used in this example requires short-axis multi-planar reformations with 5- to 8-mm MPR thickness. It provides left ventricular volumes for all loaded phases, including end-systolic (*upper left*) and end-diastolic (*upper right*) volumes for determining ejection fraction (*lower left*). A "bulls-eye plot" for display of regional wall motion can also be generated (*lower right*). (Case courtesy of Tübingen University, Germany)

ventricle is automatically segmented to allow calculation of end-systolic and end-diastolic volumes, stroke volume, and ejection fraction (Fig. 6.21). With these software tools, segmentation of the ventricular blood pool can be conveniently adjusted for standardization purposes. This is particularly helpful for assessment of the papillary muscles during calculation of left ventricular volumes. The papillary muscles are included in some functional evaluation approaches, while they are excluded in others. With the help of refined cardiac models, endocardial and epicardial contours may be automatically detected – requiring only minor user interactions for a correction – as a basis for calculating myocardial mass and for analyzing wall thickening.

6.7 Myocardial Perfusion Evaluation

Myocardial perfusion can be assessed via dynamic measurement of the enhancement of the myocardium after injection of contrast, with the goal of differentiating viable from infarcted myocardium. An enhancement curve is determined by measuring HU values in defined small regions of interest (ROIs) in thick axial slices or oblique MPRs that are acquired during ECG-triggered scans in consecutive cardiac cycles. Standard ROI-based dynamic measurement tools are currently in use for generation of such enhancement curves. As evaluation of myocar-

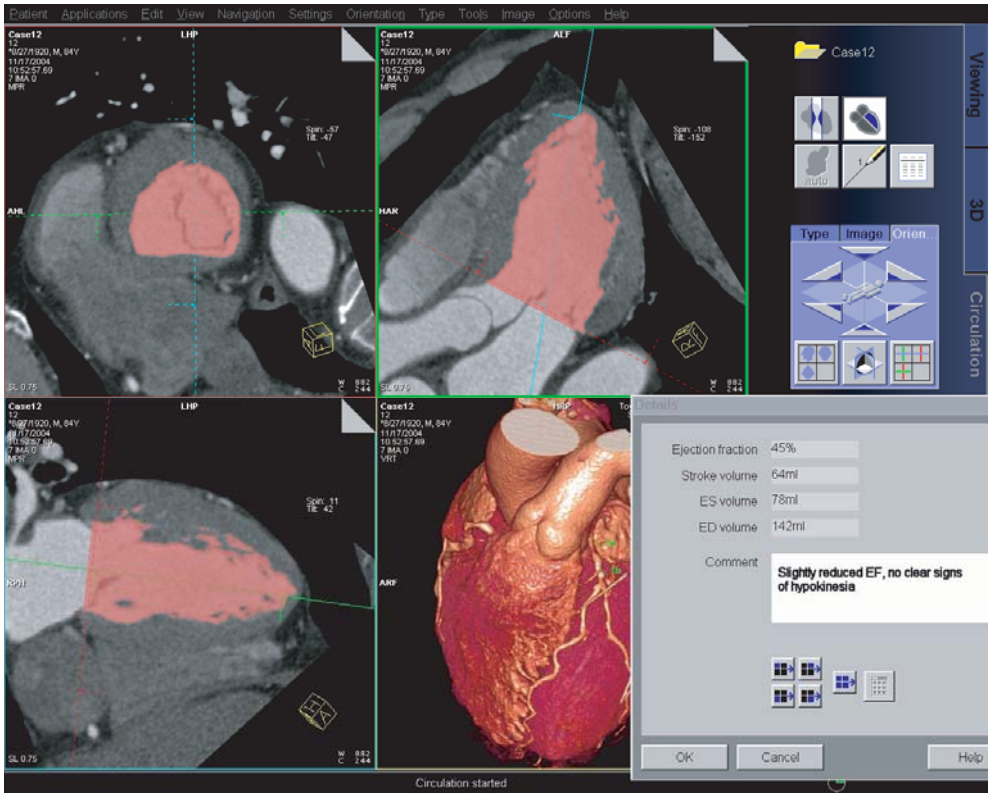

Fig. 6.21. Functional evaluation in a patient with a significant LAD stenosis, examined with a 64-slice CT scanner with 64 × 0.6-mm slices per rotation. The evaluation was done using comprehensive slice-based cardiac evaluation software. Thin-slice axial images in different phases of the cardiac cycle are needed as an input. Following manual definition of the basal plane in end-systole and end-diastole, the blood pool in the left ventricle is automatically segmented to allow calculation of end-systolic and end-diastolic volumes, stroke volume, and ejection fraction. The papillary muscles are excluded in this approach. (Case courtesy of Toyohashi Heart Center, Japan)

dial perfusion does not yet play a significant role in today's clinical practice and has not yet left the research state, this application is not yet supported by dedicated post-processing tools. The limited z-axis coverage of current multi-slice CT scanners, inherent HU value inconsistency during dynamic, ECG-triggered partial-scan acquisition, and the lack of clinical validation have hampered the establishment of myocardial perfusion measurement with multi-slice CT in clinical practice. However, initial promising clinical results have been obtained with the recently introduced fast 64-slice CT scanners, which feature faster rotation speeds and larger z-axis coverage.

Nonetheless, measurement of myocardial enhancement based on first-pass contrast enhancement is gaining attention as a potential tool to predict patient outcome after myocardial infarction (Paul 2003, Mahnken 2005b). Information on first-pass myocardial enhancement is readily available as a by-product of cardiac and coronary CT angiography examinations, similar to functional information. Figure 6.22 shows the use of a work-in-progress evaluation tool for a patient with myocardial infarction. The blood pool of the left ventricle has been segmented and removed to allow better differentiation of the subtle density changes in the myocardium. Density color-coding was applied to direct the attention of the user to areas with abnormal enhancement.

For the examination of patients with suspected myocardial infarction, the additional evaluation of

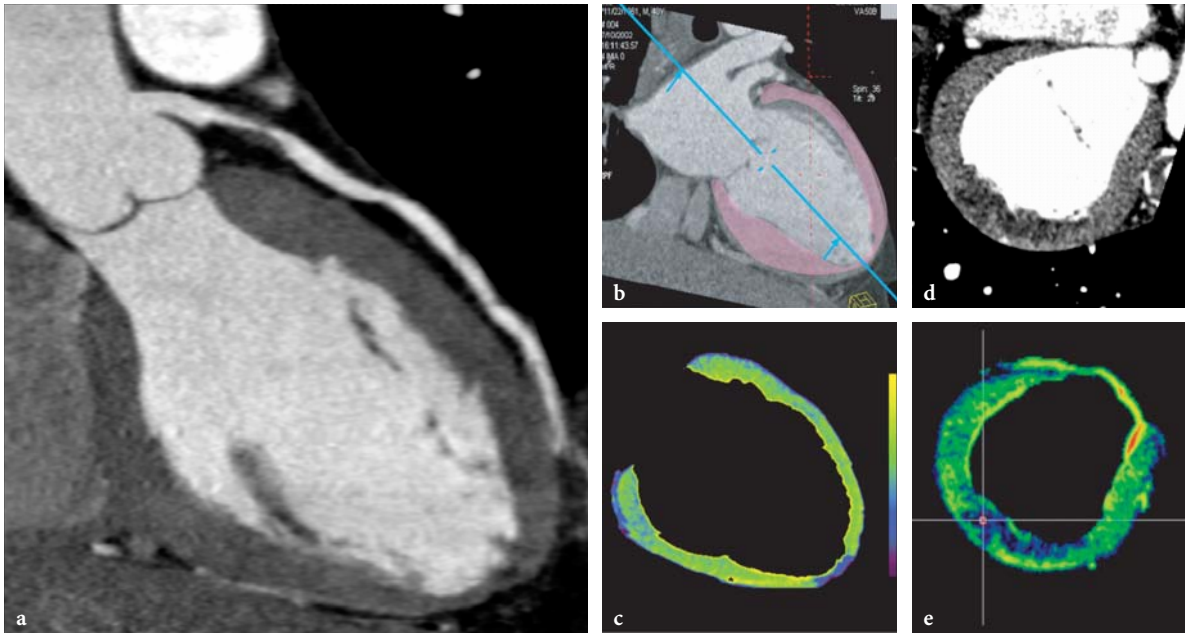

Fig. 6.22a–e. Evaluation of myocardial enhancement in a patient with suspected myocardial infarction, based on scan data acquired on a 64-slice CT scanner with 64 × 0.6-mm slices per rotation. **a** MIP reconstruction reveals a high-grade stenosis in the proximal LAD. **b**, **c** Automated segmentation of the myocardium allows the generation of a color-coded map using a work-in-progress software. Short-axis reformation allows for the evaluation of first-pass myocardial perfusion defects. **d** While the corresponding hypo-attenuated area in the myocardium can also be appreciated in the original MPR, **e** segmentation of the blood pool and color-coding facilitates (*blue color* for low perfusion) the diagnosis. (Case courtesy of Hôpital Marie Lannelongue, Paris, France)

late enhancement might be of clinical value. Visualization of late myocardial enhancement resulting from contrast leakage in infarcted myocardium requires an additional ECG-gated low-dose scan a few minutes after the first-pass cardiac or coronary CT angiography examination. While areas of hypo- or hyper-enhancement in the myocardium can also be detected in the source images, the subtle changes in HU values that have to be appreciated call for support of the user by means of advanced post-processing techniques.

6.8 Quantification of Coronary Calcification

The 3D visualization and post-processing techniques presented so far are predominantly intended for the visualization and quantitative evaluation of contrast-enhanced images from cardiac and coronary CTA examinations. The quantification of coronary calcification on the other hand is based on non-enhanced CT-images, yet it requires dedicated post-processing tools and quantification algorithms.

The earliest and still frequently used algorithm for the quantification of coronary artery calcium is the so-called Agatston score (Agatston 1990), which was developed primarily for electron beam CT (EBCT) but has been adapted for multi-slice CT protocols. The Agatston score is semi-quantitative and is based on slice-by-slice analysis of non-overlapping axial CT images. A CT-value threshold of 130 HU is commonly used for the identification of calcifications in every axial image (Fig. 6.23). All voxels in a slice that exceed this value are color-coded for an initial orientation. Among these suspicious voxels, which can represent false positives arising from image noise, the user has to manually pick the relevant coronary calcifications. Region-growing algorithms are used to identify all voxels belonging

to a lesion (Fig. 6.24). A score Ag(n) is calculated for each individual lesion n by multiplication of the area (in mm^2) with a co-factor (between 1 and 4) that depends on the HU-peak value in the considered lesion (Eq. 6.2).

$$Ag = \sum_n Ag(n) = \sum_n Area(n) \cdot CoFactor(n) \tag{6.2a}$$

$$CoFactor = \begin{cases} 1; & 130 \le Peak < 200 \\ 2; & 200 \le Peak < 300 \\ 3; & 300 \le Peak < 400 \\ 4; & Peak \ge 400 \end{cases} \tag{6.2b}$$

To reduce the influence of image noise, a minimum area $Area_{min}$ can be used to discard very small scores that probably represent noise pixels. The scores of the individual lesions are separately accumulated for the main coronary artery segments: left main (LM), LAD, CX, and RCA (Fig. 6.24). The sum of these separate scores yields a total score for the total calcified plaque burden.

The Agatston-scoring algorithm was developed for sequential image data and needs modification if overlapping slice data are processed. A straightforward approach is to calculate normalized scores AgN that are multiplied with the ratio of image reconstruction increment Inc and slice width SW (Ohnesorge 2000, Ohnesorge 2002):

$$AgN = \frac{Inc}{SW} \sum_n Area(n) \cdot CoFactor(n) \tag{6.3}$$

Due to the non-linear weighting operation with the integer variable CoFactor, the Agatston score is very prone to variations. Different studies have shown that the inter-scan variability of the scores can be more than 20% (Devries 1995, Becker 2000), particularly for small amounts of calcification; therefore, the reproducibility needs to be improved.

Alternative volumetric quantification algorithms have been developed that can process sequential and overlapping image data of different slice width as well as provide volume-equivalents (in mm^3) and mass-equivalents (in mg) of calcified plaques (Eqs. 6.4, 6.5). Non-linear operations that may increase inter-scan variability are eliminated. Isotropic interpolation procedures in between adjacent

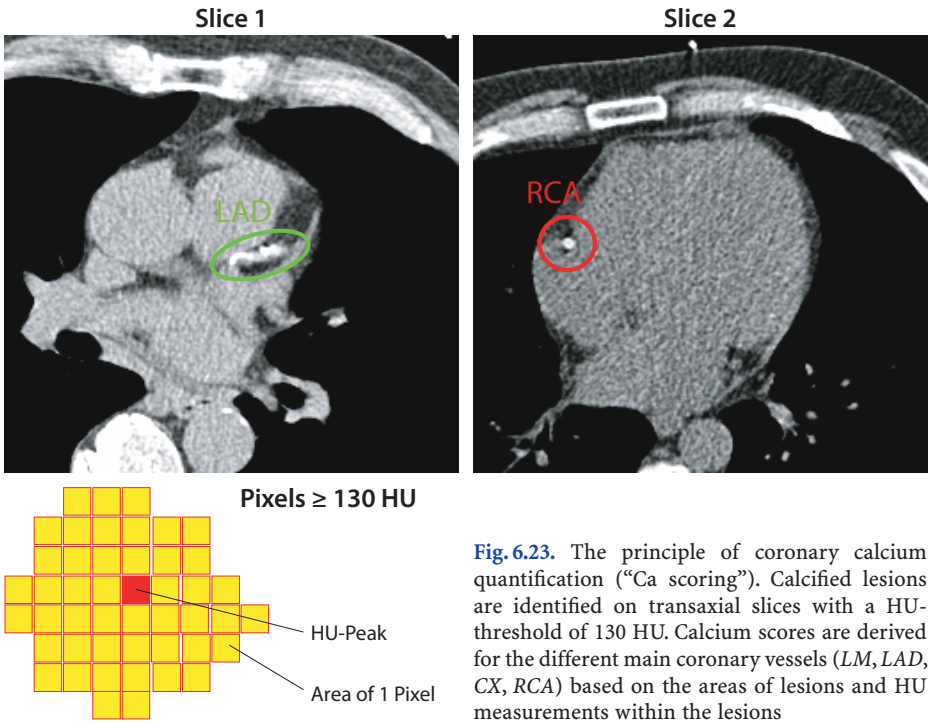

Fig. 6.23. The principle of coronary calcium quantification ("Ca scoring"). Calcified lesions are identified on transaxial slices with a HU-threshold of 130 HU. Calcium scores are derived for the different main coronary vessels (*LM*, *LAD*, *CX*, *RCA*) based on the areas of lesions and HU measurements within the lesions

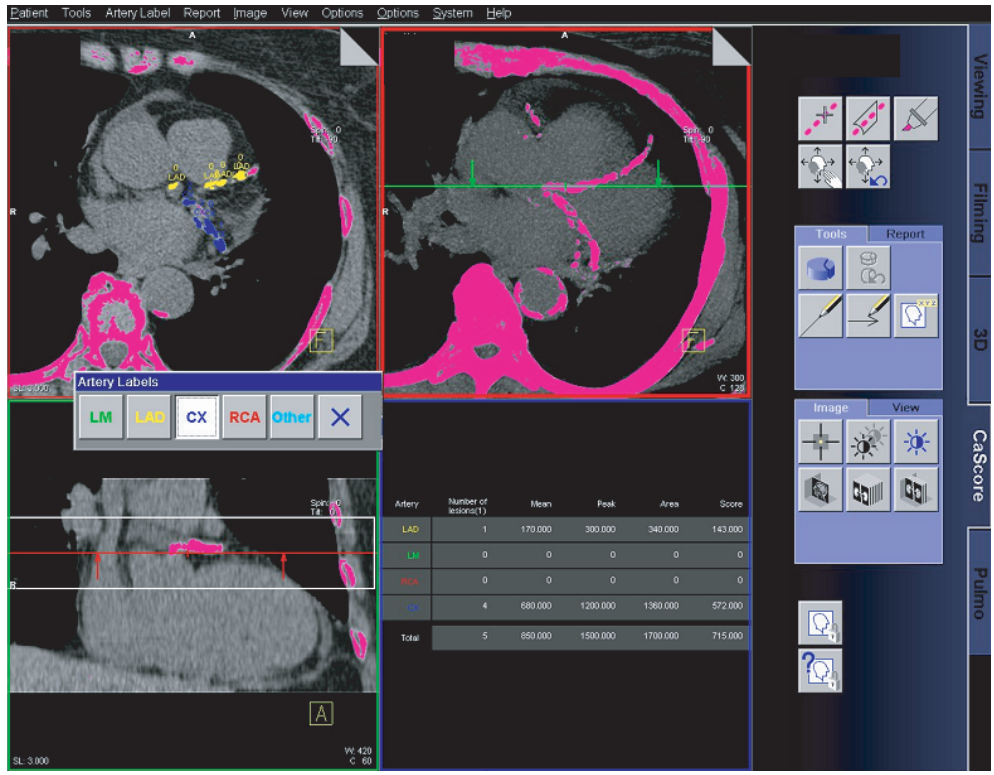

Fig. 6.24. Software platform used for the quantification of coronary calcification. Lesions exceeding the calcium threshold of 130 HU are identified with color-coding and segmented with 3D-based picking and region-growing tools. After segmentation, the lesions are assigned to the various coronary arteries (LM, LAD, CX, RCA). Coronary calcifications are quantified by means of Agatston score, calcium volume, and calcium mass calculation. Calibration factors that are pre-determined using phantom measurements and depend on the scan protocol form the basis for calculating calcium mass. The quantitative measurements are displayed and reported in table format

image slices can be used to reduce the influence of partial-volume errors for improved reproducibility (Callister 1998, Ohnesorge 2002).

$$Vol = \sum_n Vol(n) = \sum_n Area(n) \cdot Inc \tag{6.4a}$$

$$Mass = \sum_n Mass(n) \cdot = \sum_n Area(n) \cdot Inc \cdot \rho(MeanHU(n)) \tag{6.4b}$$

$$Vol_I = \sum_n Vol_I(n) = \sum_n Area(n) \cdot Inc \cdot W_I(n) \tag{6.5a}$$

$$Mass_I = \sum_n Mass_I(n) = \sum_n Area(n) \cdot Inc \cdot W_I(n) \cdot \rho(MeanHU(n)) \tag{6.5b}$$

The isotropic interpolation factor $W_I(n)$ takes information from the adjacent slices into account and modifies the contribution of a single image voxel to the score of an individual lesion. $W_I(n)$ may be greater or smaller than 1 depending on the propagation of a lesion (Fig. 6.25). Also, voxels that were not identified as part of a lesion due to a HU value < 130HU may contribute to the score of the lesion if corresponding voxels at the same image position in the adjacent

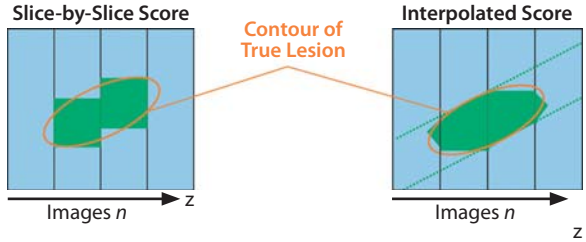

Fig. 6.25. Interpolation algorithms during volumetric quantification of coronary calcification. 3D-shaped calcified lesions may be detected in consecutive slices. Interpolation between the slices can be useful for better reproduction of the true plaque size

slice have a high contribution. A mass equivalent is calculated by multiplying the volume with a density factor ρ of the lesion. The latter is derived from the mean HU value in the plaque, which linearly depends on the mean density (in mg/mm^3). The density factor ρ and its HU value must be determined from appropriate calibration procedures (Ulzheimer 2003) for the scanner and according to the scan protocol used, and have to be included in the quantification software. A special phantom has been developed that allows for identification of calcium thresholds and calcium-mass calibration factors for different scan protocols (Fig. 6.26). The density factor ρ for an individual lesion n depends on the difference of the mean HU value in the lesion and the HU value of water as well as on a scanner- and scan-protocol-specific constant C_ρ as given in Eq. 6.6:

$$\rho(MeanHU(n)) = C_\rho \cdot (MeanHU(n) - HU_{Water}) \quad (6.6)$$

For example, for a frequently used scan protocol for a certain evaluated scanner (e.g., SOMATOM Sensation 16, Siemens, Germany with 16 × 1.5-mm collimation, 3-mm slice width, 120-kV tube voltage, 100-mA tube current), the constant C_ρ was determined by the phantom study as:

$$C_\rho = 0.84 \frac{mg}{cm^3 \cdot HU} \quad (6.7)$$

It could even be shown that, with such calibration efforts, coronary calcium mass can be accurately quantified from contrast-enhanced scans of the coronary arteries with thin-slice reconstruction, which shows increased sensitivity for smaller calcified lesions (Fig. 6.27). Based on an appropriate adaptation of the calibration factors, a high degree of correlation with the results of pre-contrast calcium scoring scan was shown (Hong 2002) (Fig. 6.28).

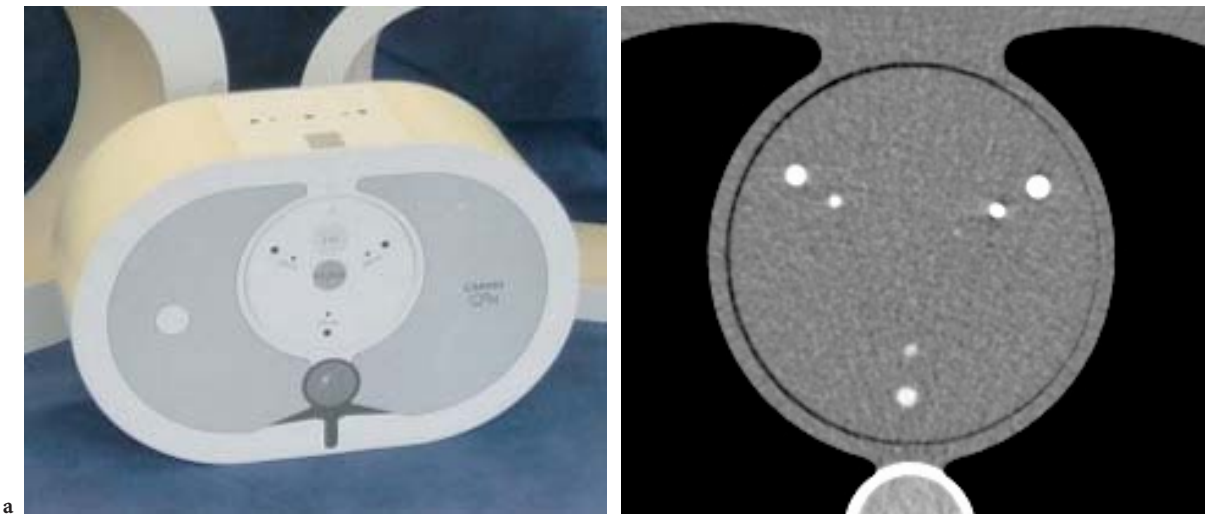

a b

Fig. 6.26. a The anthropromorphic chest phantom (Institute of Medical Physics, Erlangen, Germany and QRM, Möhrendorf, Germany) for determining the calibration factors for coronary calcium mass quantification. **b** The phantom contains a centered Lucite cylinder that simulates the heart and includes calibration inserts and calcium hydroxyapatite inserts of different dimensions and density that can be displayed in axial slices

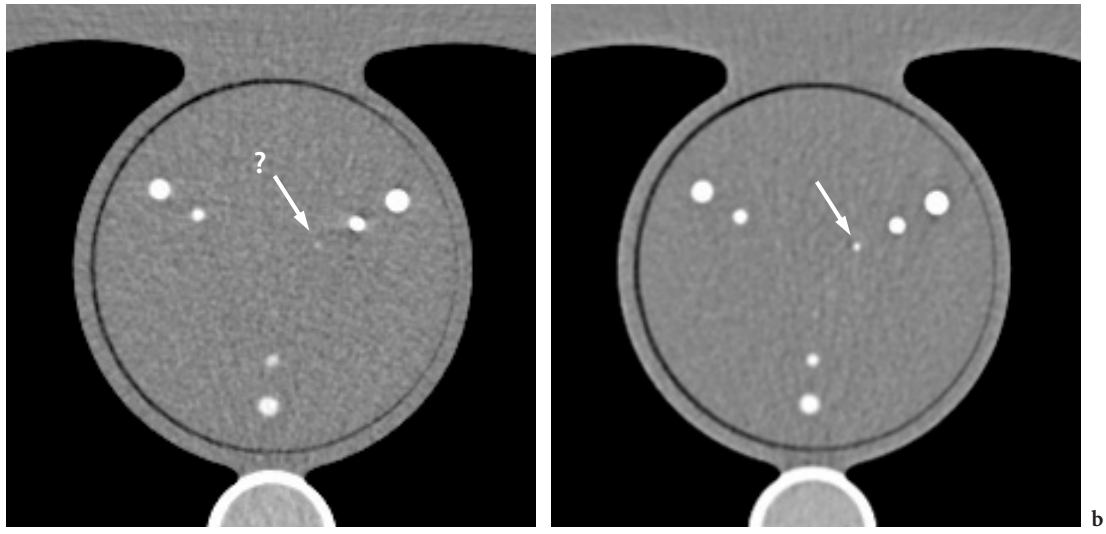

Fig. 6.27. Calibration phantom scanned with ECG-gated spiral acquisition on a 16-slice CT scanner using a 16 × 1.5-mm collimation, 3.0-mm slice width and b 16 × 0.75-mm collimation, 1.0-mm slice width. Smaller lesions can be identified with 1.0-mm slice width (smallest detectable lesion: 0.6 mg calcium hydroxyapatite; *arrows*). The best agreement between calcium mass detected with 1.0-mm slice width and that detected with 3.0-mm slice width and 130 HU threshold was achieved using a calibration coefficient C_ρ = 0.84 mg/(cm^3·HU) for the 3-mm slice-width and C_ρ = 0.88 mg/(cm^3·HU) at a modified calcium threshold of 350 HU for a 1.0-mm slice width

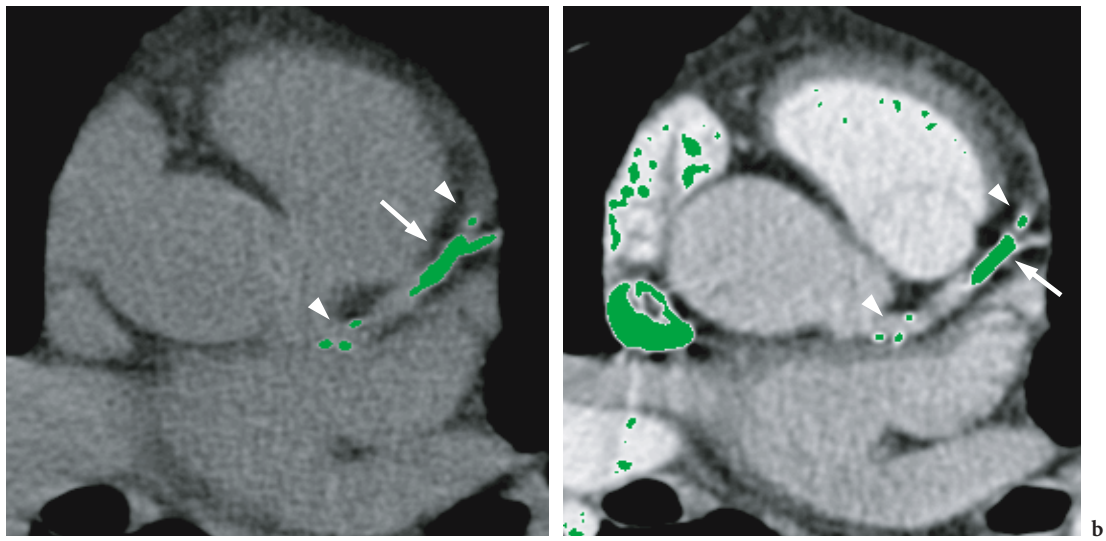

Fig. 6.28a, b. Examination of a 57-year-old male with calcified coronary artery plaques. **a** Spotty calcifications in the left main stem (*arrowheads*) and long calcifications in the mid-segment of the LAD (*arrow*) can be detected in the non-enhanced coronary calcium scan with 3.0-mm slice width and a 130-HU calcium threshold. **b** The same spotty calcifications (*arrowheads*) and long calcification (*arrow*) can be detected in the contrast-enhanced high-resolution scan with 1.25-mm slice width and 350-HU calcium threshold

The Agatston algorithm for quantification of coronary calcification is still frequently used. However, the Agatston score and the closely related acquisition parameters may not be an appropriate basis for coronary calcium quantification with a wide spectrum of different acquisition systems. With the advent from different manufacturers of multislice CT scanners with different scan parameters, cross-technology quality control and calibration methods gain importance. The most promising approach to establish a cross-industry standard is to use absolute mass quantification, which can include different scanner properties and protocol variations via phantom calibration (Hong 2002, Ulzheimer 2003). Moreover, recent studies indicate that the use of quantitative mass measurement provides better results for inter-scan and inter- and intra-observer variability than obtained with the traditional Agatston scoring method (Ohnesorge 2002). Therefore, assessing coronary artery calcification by evaluating absolute calcium mass shows great potential for increasing the accuracy, consistency, and reproducibility of coronary calcium measurements (Ulzheimer 2003) and will replace the traditional Agatston scoring system in the near future.

References

Addis KA, Hopper KD, Iyriboz TA, Liu Y, Wise SW, Kasales CJ, Blebea JS, Mauger DT (2001). CT angiography: in vitro comparison of five reconstruction methods. AJR 177: 1171–1176

Agatston AS, Janowitz WR, Hildner FJ, Zusmer NR, Viamonte M, Detrano R (1990). Quantification of coronary artery calcium using ultrafast computed tomography. JACC 15, 827–832

Becker CR, Jakobs TF, Aydemir S, Becker A, Knez A, Schöpf UJ, Brüning R, Haberl R, Reiser MF (2000). Helical and single-slice conventional CT versus electron beam CT for the quantification of coronary artery calcification. AJR 174:543–547

Callister TQ, Cooil B, Raya SP, Lippolis NJ, Russo DJ, Raggi P (1998). Coronary artery disease: improved reproducibility of calcium scoring with an electron-beam CT volumetric method. Radiology 208:807–814

Devries S, Wolfkiel CJ, Shah V, Chomka E, Rich S (1995). Reproducibility of the measurement of coronary calcium with ultrafast ct. Am J Cardiol 75:973–975

Feyter de PJ, Krestin GP (2005). Computed tomography of the coronary arteries. Chapter 2: Image post-processing. Taylor & Francis, Oxfordshire, UK

Flohr T, Stierstorfer K, Raupach R, Ulzheimer S, Bruder H (2004). Performance evaluation of a 64-slice CT-system with z-flying focal spot. Röfo Fortschr Geb Rontgenstr Neuen Bildgeb Verfahr. 176:1803–1810

Hong C, Becker,CR, Schöpf UJ, Ohnesorge B, Brüning R, Reiser MF (2002). Coronary artery calcium: absolute quantification in non-enhanced and contrast-enhanced multidetector-row CT studies. Radiology 223:474–480

Leber AW, Knez A, Becker A, Becker C, Ziegler F, Nikolaou K, Rist C, Reiser MF, White C, Steinbeck G, Boekstegers P (2004). Accuracy of multidetector spiral computed tomography in identifying and differentiating the composition of coronary atherosclerotic plaque. JACC 43(7): 1241–1247

Leber AW, Knez A, Ziegler F, Becker A, Nikolaou K, Paul S, Wintersperger B, Reiser MF, Becker C, Steinbeck G, Boekstegers P (2005). Quantification of obstructive and non-obstructive coronary lesions by 64-slice computed tomography. JACC 46(1)

Mahnken AH, Wildberger JE, Sinha AM, Dedden K, Stanzel S, Hoffmann R, Schmitz-Rode T, Günther RW (2003). Value of 3D-volume rendering in the assessment of coronary arteries with retrospectively ecg-gated multislice spiral CT. Acta Radiologica 44(3): 302 ff.

Mahnken AH, Katoh M, Bruners P, Spuentrup E, Wildberger JE, Günther RW, Buecker A (2005a). Acute myocardial infarction: assessment of left ventricular function with 16-detector row spiral CT versus MR imaging – study in pigs. Radiology 236:112–117

Mahnken AH, Koos R, Katoh M, Wildberger JE, Spuentrup E, Buecker A, Günther RW, Kühl HP (2005b). Assessment of myocardial viability in reperfused myocardial infarction using 16-slice computed tomography in comparison to magnetic resonance imaging. JACC 45 (12): 2042–2047

Ohnesorge B, Knez A, Becker CR, Schröder S, Kopp AF, Fischbach R, Haberl R, Reiser MF (2000). Reproducibility of coronary calcium scoring with EBCT and ECG-gated multislice spiral CT (Abstract). Circulation 102(18):II-398–399

Ohnesorge B, Flohr T, Fischbach R, Kopp AF, Knez A, Schröder S, Schöpf UJ, Crispin A, Klotz E, Reiser MF, Becker CR (2002). Reproducibility of coronary calcium quantification in repeat examinations with retrospectively ECG-gated multisection CT. Eur Radiol 12:1532–1540

Ooijen van PMA, Ho KY, Dorgelo J, Oudkerk M (2003). Coronary artery imaging with multidetector-row CT: visualization issues. Radiographics 23: e16

Paul JF, Dambrin G, Caussin C, Lancelin B, Angel C (2003). 16-slice computed tomography after acute myocardial infarction – from perfusion defect to culprit lesion. Circulation 108:373–374

Prokop M, Shin HO, Schanz A, Schaefer-Prokop CM (1997). Use of maximum intensity projections in CT angiography: a basic review. Radiographics 17(2):433–51

Raman R, Napel S, Rubin D (2003). Curved slab maximum

intensity projection. method and evaluation. Radiology 229:255–260

Rankin CS (1999). CT angiography (Review). Eur Radiol 9: 297–310

Rubin GD, Napel S, Jeffrey RB Jr (1993). STS-MIP: a new reconstruction technique for CT of the chest. J Comput Assist Tomogr 17(5):832–838

Schroeder S, Kopp A, Baumbach A, Meisner C, Kuettner A, Georg C, Ohnesorge B, Herdeg C, Claussen C, Karsch K (2001a). Noninvasive detection and evaluation of atherosclerotic coronary plaques with multi-slice computed tomography. JACC 37(5): 1430–1435

Schroeder S, Flohr T, Kopp AF, Meisner C, Kuettner A, Herdeg C, Baumbach A, Ohnesorge B (2001b). Accuracy of density measurements within plaques located in artificial coronary arteries by X-ray multislice CT: results of a phantom study. J Comput Assist Tomogr 25(6): 900–906

Vogl TJ, Nasreddin DA, Diebold T, Engelmann K, Ay M, Dogan S, Wimmer-Greinecker G, Moritz A, Herzog C (2002). Techniques for the detection of coronary atherosclerosis: multi-detector row CT coronary angiography. Radiology 223:212–220

Ulzheimer S, Kalender WA (2003). Assessment of calcium scoring performance in cardiac computed tomography. Eur Radiol 13 :484–497